Mass Loading
and
Stokes Number Effects
in
Steady and Unsteady
Particle-laden Jets

M.Eng. Science Thesis

Richard J. Foreman

The University of Adelaide

The School of Mechanical Engineering

June 2008

Chapter 3

Measurements of particle distributions in a particle-laden turbulent axisymmetric jet

3.1 Introduction

Planar imaging techniques have been used in previous studies to provide qualitative understanding and physical insight into the instantaneous spatial distribution of particles in two phase turbulent flows. Planar imaging refers to the method whereby a thin sheet of light, usually from a laser, is directed through a cross-section of the flow containing particles (or molecules). The scattered light is then captured by some detector, usually a CCD, with the light intensity a function of the particle diameter. The result is a two dimensional image showing the distribution of particles (or molecules) throughout the imaged cross-section.

For example, with this method Lazaro and Lasheras (1989) were able to visualise the orderly radial dispersion of droplets in a plane shear layer. Longmire and Eaton (1992), Eaton and Fessler (1994) showed that particles

with a Stokes number of O(1) would preferentially concentrate in the low vorticity regions between large scale structures (particle clustering), in a turbulent axisymmetric jet. Wark, Eickmann and Richards (2000) detected the presence of droplet clusters in acoustically forced reacting and non-reacting jets. The clusters were deduced to result from the large scale coherent structures formed in the near field. The presence of particle clustering in industrial flames was detected also by Smith *et al.* (2002) from the flow from a precessing jet nozzle (see Chapter 4). A practical realisation of enhanced particle clustering is thought to be a favourable combustion performance in some applications (Smith *et al.*, 1998a).

While those studies provided valuable instantaneous data as well as further conceptual understanding, there has yet to be reported basic light scattering measurements of the mean distribution of particles in an axisymmetric jet as a function of fundamental dimensionless parameters, the exit mass loading, ϕ_o, the exit Stokes number, St_o and the gas phase density ratio, ρ_j/ρ_a, where ρ_j and ρ_a and the jet and ambient air densities, respectively. The investigation of the effects of these parameters on the distribution of particles in a particle-laden jet is the subject of the current chapter.

3.1.1 Mass loading effects

Chapter 2 identified that the gas phase centreline velocity and half width may be scaled by the function $x/D(1 + \phi_o)^{-n}$, where $n = 1/2$ or 1, depending on the value of St_o. The proposed scaling was found to collapse the gas phase centreline velocity and half width data from most studies of particle-laden jets (e.g. Sheen *et al.*, 1994, Hardalupas *et al.*, 1989, Shuen *et al.*, 1985, Modarress *et al.*, 1984a,b, Laats and Frishman, 1970 and Laats, 1966). The solid phase centreline and half width properties, such as the mass flux (Laats and Frishman, 1970, Wall *et al.*, 1982, Subramanian and Raman, 1984) and concentration (Ferrand *et al.*, 2001) were also found to scale similarly to the gas phase. In the present investigation, the effect of ϕ_o on particle distri-

butions (by Mie scattering) is investigated primarily to determine whether the scaling described in Chapter 2 is applicable for said distributions. In other words, it is the aim to determine whether half widths and centreline values scale by power-law functions. To the author's knowledge, no such measurements have been reported previously in an axisymmetric jet laden with particles for a variation in ϕ_o in the two-way coupling regime.

3.1.2   Stokes number effects

The importance of the Stokes number in describing the effect of particles on the gas phase has been illustrated in Chapter 2. However, as already discussed in Chapter 1 (see Figure 1.14), St_o is the parameter that governs the distribution of particles in flows, especially those with large scale turbulent structures. Mass flux data presented already in Figure 1.14, indicate that, for small St_o, a rise in particle 'concentration' downstream from the jet exit (Laats and Frishman, 1970), the so called 'pinch-effect' (Frishman *et al.*, 1997), will occur. Frishman *et al.* (1997, 1999) have investigated the the 'pinch-effect' numerically and found that, to satisfactorily predict this phenomena, one must consider many physical aspects contributing to the development of the flow within the pipe and in the jet near field. Aspects to be considered include the particle size distribution (PSD), the Magnus, Saffman and turbophoresis forces, as well as particle-particle and particle-wall interactions within the pipe. The neglect of any of these aspects results in the failure to satisfactorily predict the pinch-effect. Here, an investigation into the dependence of the axial location of the pinch effect, x_p, on the Stokes number and ϕ_o is also undertaken.

The pinch-effect is related to the distribution of dynamics of particles within the pipe. Hussainov *et al.* (1996) have investigated this effect more closely and determined that the qualitative shape of the exit profiles is governed by the exit Stokes number based on the friction velocity St_o^* (see equation 3.1 below). According to those authors, as well as Frishman *et al.*,

(1997), a concave distribution in the exit profile is produced for $St_o^* < 1$, i.e. the concentration maximum is located close to the wall. In contrast, a convex profile is produced for $St_o^* > 1$, i.e. the maximum is found on the centreline. These effects are related to the slip velocity (velocity difference between gas and solid phase) in the pipe, which is found to be significant if $St_o^* > O(3)$. The dependence of the shape of the concentration profile at the exit of the pipe on St_o^* is also investigated here. Experiments are performed for $St_o^* > 1$, $St_o^* < 1$ and $St_o^* \sim 1$. As all those regimes are less than $St_o^* = 3$, the pinch-effect will be detected in them all (Frishman *et al.*, 1997). This is in contrast to the 'scattering effect', or the rapid dispersion of particles downstream from the jet exit as shown in Figure 1.14 for larger St_o. Figure 1.14 also showed that the centreline decay rate of mass flux is reduced for a rise in St_o. The centreline decay rate of particles distributions, as well as their spread, will also be investigated for a range of St_o^*.

3.1.3 Variable density effects

The effect on particle distributions when the gas phase density is different from its surroundings is investigated also. In many practical practical particle-laden flows, the jet is often of a different density from that of its surroundings. For example, most pulverised fuels are transported by air that is slightly heated relative to ambient, but much cooler than the combustion air. The scaling regimes of single phase, variable density jets have been detailed in Chen and Rodi (1980). The equivalent (or 'effective') diameter may account for the variation in centreline velocity with density ratio, ρ_j/ρ_a. For $\rho_j/\rho_a > 1$, the centreline decay rate is reduced while for $\rho_j/\rho_a < 1$, it is increased. However, unlike in particle-laden jets where jet spread is reduced for an increase in ϕ_o, no clear dependence of the half width on ρ_j/ρ_a exists in single-phase variable density jets (Richards & Pitts, 1993). Despite the breadth of applications in this field, to the author's knowledge, no previous studies in non-reacting, particle-laden, variable density axisymmetric jet have been reported. Nevertheless, a numerical study was performed by Soteriou

and Yang (1999) of a particle-laden plane shear layer. The parameters varied in that study included the Stokes number, velocity, density and viscosity ratios. They found the maximum absolute particle dispersion to occur for an exit Stokes number of unity and for a unity density ratio. However, it is important to note that this work is yet to be validated. Hence a clear need is present for experimental data in variable density, particle-laden free shear flows.

3.1.4 Summary

This chapter aims to assess the effect of the variation of the parameters, ϕ_o, St_o^* and ρ_j/ρ_a on the distribution of particles in a turbulent axisymmetric jet is investigated. In particular: it is the aim to (i) determine whether particle distributions for a variation in ϕ_o, scale similarly to the gas phase velocity; (ii) investigate the dependence of St_o^* and ϕ_o on the location of the maximum axial concentration, the pinch-effect, and the shape of the exit profiles; (iii) investigate the dependence of centreline distributions and half widths on St_o^* and (iv) determine the effect of density ratio of the gas phase on the centreline distributions and half widths.

3.2 Experimental Details

3.2.1 Experimental Conditions

Details of experimental conditions are shown in Table 3.1. Exit stokes numbers, St_o, ranging from 4-20, mass loadings ϕ_o, ranging from 0.19-0.66 and two density ratios, $(\rho_j/\rho_a = 0.87$ and $1)$ are investigated. The exit Stokes number based on the friction velocity is defined after Hussainov *et al.* (1996) as

$$St_o^* = \frac{\rho_p d_p^2 u^*}{18\mu D}.$$ (3.1)

St_o	St_o^*	Re	D(mm)	U(m/s)	$d_p(\mu$m)	ρ_p(kg/m^3)	ϕ_o	ρ_j/ρ_a
11	1	72000	13.5	80-85	29.2	700	0.19-0.66	0.87-1
20	3	72000	13.5	80	27.7	2500	0.53-0.70	1
4	0.4	76000	22	52	29.2	700	0.1-0.45	1

Table 3.1: Details of the experimental conditions.

Here, u^* is the friction velocity, defined as

$$u^* = \left(\frac{\tau_w}{\rho}\right)^{1/2}, \tag{3.2}$$

where τ_w is the wall shear stress. For the present experiments, the friction velocity, u^* has been estimated from the Blasius equation (Schlichting, 1960),

$$\left(\frac{u^*}{U}\right)^2 = 0.03955 Re^{-1/4}. \tag{3.3}$$

On this basis, $St_o^* = 1$, 3 and 0.4.

The Stokes numbers have been varied by changing the pipe diameter (13.5 and 22mm) and particle type. The jet velocity was maintained as high as possible so that the velocity ratio between the jet and the co-flow (see below) was maximised. That way a linear gas phase jet spread can be anticipated (Rajaratnam, 1976). The particles used were the commercially available Qcel 5070s hollow glass spheres (particle density, $\rho_p = 700$kg/m^3) and Spheriglass 3000 solid glass spheres ($\rho_p = 2500$kg/m^3) from Potters Industries Inc., with a size distribution as measured with a Malvern Mastersizer 2000 displayed in Figure 3.1. Their respective mass/volume weighted mean diameters (d_{43}) are 29.2 and 27.7μm. A submicron mode is evident in the Spheriglass 3000 distribution. It is unclear whether this is an artifact of the measurement technique or that fragments of glass are present as a consequence of the particle manufacturing. Fortunately, this mode only represents approximately 5% of the total mass fraction and thus its presence does not affect d_p significantly.
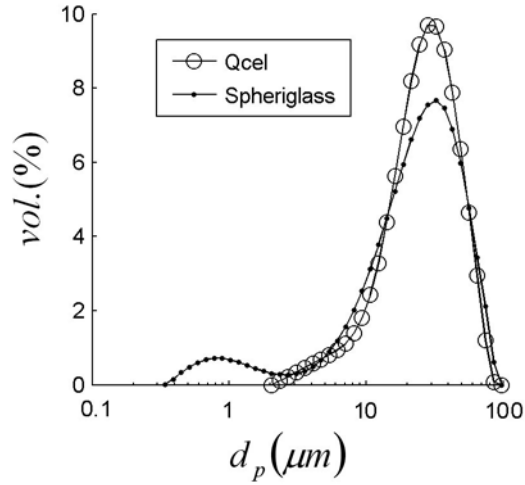
Figure 3.1: Qcel 5070s and Spheriglass 3000 particle size distribution.

3.2.2 Apparatus

Figure 3.2 shows the experimental apparatus, with key features of the particle delivery and flow development systems. Regulated compressed air feeds both the main line to the nozzle and the line prior to the fluidised bed. The fluidised bed was mounted on a fulcrum and placed over a load cell for measurement of the particle mass flow rate, $\dot{m}_p$, which is linear with time to within 0.2% (based on a linear correlation coefficient). A reference weight of 100g was used to calibrate the system. Particles were drawn from the fluidised bed into the main line via a venturi. The length of the pipes were approximately 2m and its internal diameters were 13.5 and 22mm, so that $L/D \approx$ 150 & 91, sufficient to closely approximate fully developed single phase flow at the jet exit. Earthing wires were attached to the pipe to discharge any static electricity. A conical diffuser with an included angle of 12.5° and 15° were fitted to the outside of the pipes, finishing some 11 and 9 diameters upstream from the pipe exit. This is to provide a smooth transition between an outer tube designed to accommodate a larger diameter pipe than the present ones. The pipes are aligned on the axis of a 650mm square working section of an open loop tunnel. Flow conditioning comprised five consecutive screens, straws and a bell mouth that reduces swirl and background turbulence within
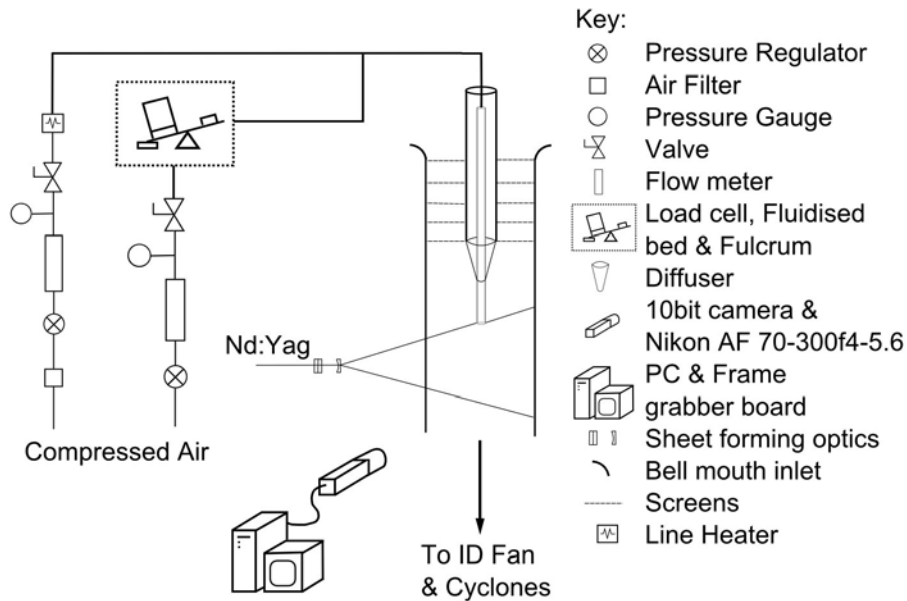
Key:
- ⊗ Pressure Regulator
- □ Air Filter
- ○ Pressure Gauge
- ⋈ Valve
- ▯ Flow meter
- Load cell, Fluidised bed & Fulcrum
- ▽ Diffuser
- 10bit camera & Nikon AF 70-300f4-5.6
- PC & Frame grabber board
- ▯▯ Sheet forming optics
- ⟍ Bell mouth inlet
- ----- Screens
- ⊡ Line Heater

Nd:Yag

Compressed Air

To ID Fan & Cyclones

Figure 3.2: A schematic diagram of the air and particle feeding systems, working section and optical arrangement.

the working section. An induced draught fan provided the motive force for the tunnel and delivered the particle-laden flow to a bank of cyclones. A co-flow velocity of approximately 2.5m/s was measured with a Pitot-static probe. Previous measurements with a mean tunnel velocity of 8m/s have determined the uniformity to be $\pm 3.8\%$ (Birzer $et\ al.$, 2007).

A line heater downstream from the main valve, as shown in Figure 3.2, was used to vary the density of the air. Because of limitations associated with the equipment, the maximum supply temperature of the jet was approximately 60°C, with an ambient temperature of 18°C. The temperature was measured with a thermocouple placed at the jet exit. To avoid the need to place an intrusive probe near to the jet, the exit temperature was calibrated against the voltage of the line heater. Measurements of a particle-laden stream revealed that the temperature was reduced by approximately 5°C for $\phi_o = 0.62$ and the jet density was corrected for this.

76

3.2.3 Optics

Figure 3.2 also shows sheet forming and collection optics. A Nd:Yag, 10Hz pulsed, 532nm Quantel laser was used to produce a sheet of approximately 0.5mm thickness (for $St_o = 4$, sheet thickness was approximately 2mm) using appropriate optical components. An imaged area of approximately 350mm × 350mm was obtained via a NIKON AF 70-300mm f4-5.6 zoom lens onto a 10bit CCD array of 1008 × 1018 pixels to provide a spatial resolution of approximately 0.35mm in the image plane. The scattered signal, S, is proportional to the sum of the squared diameter of particles within each measurement volume (see Figure 1.18). The effects of light sheet attenuation are discussed in conjunction with data presented below. To avoid pixel saturation, f-stops of between 11 and 22 were used depending on the mass loading. Pixel saturation was assessed by finding the percentage of pixels on the jet centreline that are saturated. This was found to be less than 4% for the worst case which is within the overall measurement uncertainty. Small differences (3% at the image edges) in the spatial variation of light imaged on the CCD, measured with a blank sheet for different f-stops, were detected. Corrections for this were not applied since it is thought that this would introduce comparable errors from imperfect illumination of a blank sheet.

3.2.4 Post-processing

For each case, 200 instantaneous images were saved on a frame grabber board. Each image was corrected for variations in laser sheet profile, camera gain, collection optics, CCD noise (electronic plus background) and laser shot variation. Light sheet correction images were obtained by filling the working section with smoke and illuminating with laser light at the same power as that of the experiments. To compensate for the weaker scattering of the smoke, the f-stop used in obtaining the 200 smoke images was set to 4. A background correction was made by subtracting a mean background image. A 10 pixel

region of the image corresponding to the uniform reflection from the pipe was used to correct for laser shot variation. It was found that the camera was misaligned with the axis by 0.8°. Mean images were therefore rotated in the opposite direction of misalignment to compensate for this. Pixel saturation was assessed by finding the percentage of pixels on the jet centreline that are saturated. This was found to be less than 4% for the worst case which is within measurement uncertainty. Highly noisy mean images were encountered, most likely due to marker shot noise because of the thin light sheet. A 2 pass, 20 point moving average filter applied to the centreline variations and half widths was found to remove much of the noise.

3.3   Results

3.3.1   The variation of ϕ_o

The variation of ϕ_o for the case $St_o^* = 1$ is considered first followed by the case $St_o^* = 0.4$. In this section, the dependence of centreline values and half widths on ϕ_o and their subsequent scaling are the primary focus.

3.3.1.1   The case, $St_o^* = 1$

Shown in Figure 3.3(a) is the mean image for the case $\phi_o = 0.19$. From this image it can seen that the maximum scattered signal, i.e the 'pinch effect' (Frishman *et al.*, 1997), as discussed above, occurs downstream from the jet exit at an axial position, x_p/D corresponding to $x_p/D \approx 8$. However, particles also begin to spread near to the nozzle exit plane, and this continues with increasing axial distance. Exit profiles, normalised by the centreline value, $S_{c,o}$, for all cases, are shown in Figure 3.3(b). The light sheet in Figure 3.3(a) enters the image from the left. The exit profile for the case $\phi_o = 0.19$ is consistent with the effects of attenuation superimposed on a top
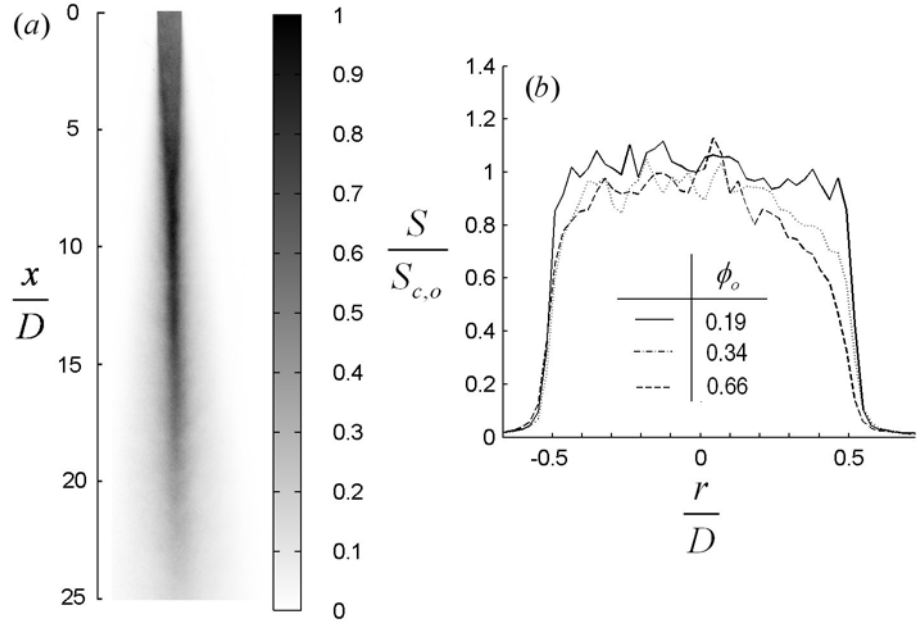
Figure 3.3: (a) Mean image of particle distributions for the case $\phi_o = 0.19$ and (b) exit profiles for three ϕ_o.

hat profile. Closer inspection of Figure 3.3(b) reveals that the profile closely approximates a top hat for the lighter loading case, $\phi_o = 0.19$, and that the signal decreases with increased r/D as ϕ_o is increased. This is entirely consistent with the departures from the top hat being caused by attenuation. Here, a flat exit profile has been found to occur when the exit Stokes number, based on the friction velocity, $St_o^* \approx 1$. The difference in magnitude of the mean exit profiles over the range $-0.4 < r/D < 0.4$ is approximately 20% for the case $\phi_o = 0.66$. However, over the range $-0.5 < r/D < 0$, the signal is approximately constant, especially for the case $\phi_o = 0.19$. The high level of fluctuations is deduced to be caused by marker shot noise (Long et al., 1981). Marker shot noise is a result of a high variation in the number of particles in each pixel volume with time, i.e. when the distribution of particles within the measurement volume begins to depart significantly from a continuum. The noise increases with reduced probe volume (including sheet thickness) and increased particle clustering. The magnitude of the fluctuations at the exit here is approximately 10% peak-to-peak.
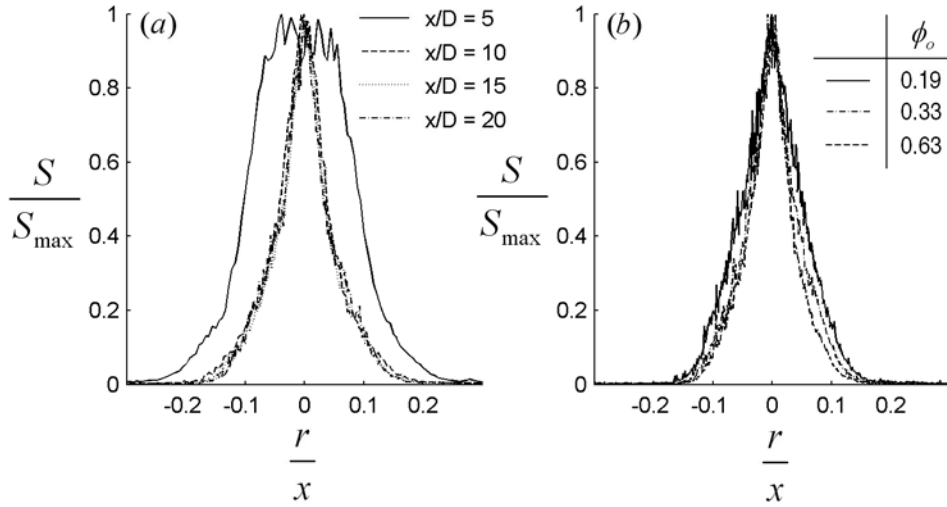
Figure 3.4: (a) Radial profiles for the case $\phi_o = 0.19$ at various x/D and (b) a comparison for three cases of ϕ_o at $x/D = 25$.

Shown in Figure 3.4(a) are the radial profiles for the case $\phi_o = 0.19$. The data are normalised by the maximum signal value, S_{max} at that particular axial location and the radial coordinate by the axial distance, x. Self-similarity of the mean velocity field is achieved by $x/D \approx 10$. The departure from self similarity in the near field at $x/D = 5$ is expected even for a gas phase. Figure 3.4(b) shows the normalised radial profiles at $x/D = 25$ for the cases $\phi_o = 0.19$, 0.34 and 0.66. At this axial location, the spread of the profiles decreases with increasing ϕ_o. Because the characteristic timescale of the flow increases with x/D, particles become increasingly responsive to the motion of the gas phase as x/D is increased (e.g. Figure 2.2). Since jet spread is reduced for an increase in ϕ_o, the spread of the more responsive particles is also reduced beyond the near field for an increase in ϕ_o.

The reduction in spread of radial profiles with increased ϕ_o is evident in the half widths shown in Figure 3.5(a). Also shown in that figure is the mean Stokes number defined following Hardalupas *et al.* (1989) to be

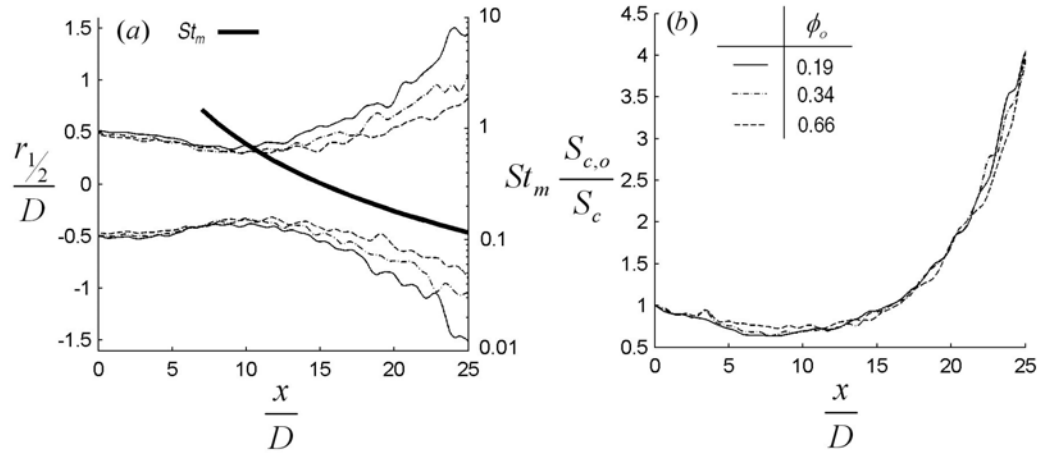$$St_m = 6.57 St_o \left(\frac{D}{x} \right).$$ (3.4)

80

Figure 3.5: (a) Half widths, including the mean Stokes number, St_m calculated according to equation 3.4, based on $St_o = 11$. (b) Centreline values, S_c, normalised by the exit value, $S_{c,o}$.

It can be seen that half widths begin to show a dependence on ϕ_o at the critical location, where $St_m \approx 1$. Particle distributions exhibit a narrowing region immediately downstream from the exit. The narrowing of half widths corresponds to the location of the pinch-effect in Figure 3.5(b). The peak axial value in $S_c/S_{c,o}$ occurs at an axial position of $x/D \approx 8$ and its magnitude is approximately 60% greater than the exit value for the case $\phi_o = 0.19$. Most significantly from Figure 3.5, the dependence of S_c on ϕ_o is only very weak for the axial range investigated.

It may appear to be contradictory that the spread exhibits a clear dependence on ϕ_o while the apparent centreline concentration does not. However, this can be explained by reference to the cumulative particle size distribution (PSD) and the calculated nominal axial distance at which particles develop a significant response to the flow (Figure 3.6). This is estimated as the value of x/D where $St_m = 1$, $x/D(St_m = 1)$. It can be seen that by $x/D = 10$, 75% of the mass of particles are partially responsive to jet spread, while at $x/D = 20$, all particles are partially responsive. The location, $x/D(St_m = 1)$ is found by rearranging equation 3.4. Hence, many particles can be expected to exhibit, at best, only a partial response to the flow in the measurement
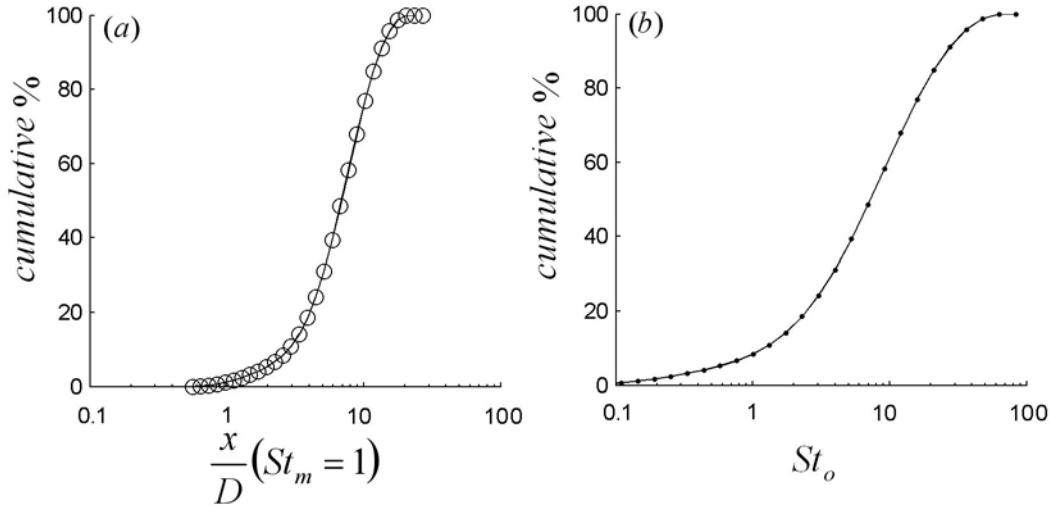
81

Figure 3.6: Cumulative size distribution, based on the PSD of Figure 3.1 for (a) the axial distances at which $St_m = 1$, indicating transition to nominal particles response to the flow and (b) the exit Stokes number, St_o.

regime. Further, since the measurement is proportional to d_p^2, the larger particles, where present, will dominate the signal. Nevertheless, 75% of particles have $St_m < 1$ by $x/D = 10$ and can be expected to exhibit reasonable response to the mean flow, and increasingly so as x/D increases.

Previous experimental (e.g. Fan *et al.*, 1990) and numerical (Luo *et al.*, 2006) studies have found that, on average, the larger particles of a distribution will concentrate on the centreline. In their direct numerical simulations, Luo *et al.* (2006) calculated that particles of $St_o = O(10)$, similar to the mass mean particle size for this case, will concentrate on the centreline. As can be seen in Figure 3.6(b), approximately 60% of the present particles have St_o less than or equal to this value. Hence, a significant mass fraction of larger particles will preferentially concentrate on the jet centreline explaining why the present centreline decay is approximately independent from ϕ_o.

Further evidence of the preferential response of particles to the flow based on their diameter is found in instantaneous images of Figure 3.7 for the cases $\phi_o = 0.19$ (a) and $\phi_o = 0.66$ (b). It is clear that beyond the 'pinch-point'
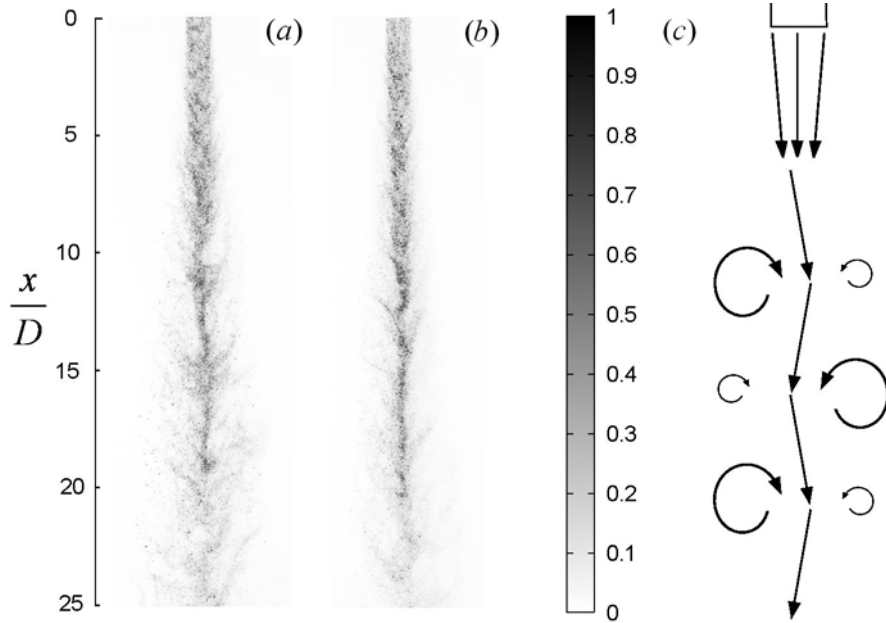
Figure 3.7: Instantaneous images for the cases (a) $\phi_o = 0.19$ (a) and (b) 0.66 showing particles preferentially distributed in a relatively thin region along the centreline, suggesting only partial response to underlying large scale motions as illustrated schematically in (c).

$(x/D \approx 8)$, a significant fraction of the particles concentrate near to the centreline on an instantaneous basis. The particles though, exhibit at least a partial response to the large structures. The deflection of the central particle stream is clearly evident in Figure 3.7(a), just above and below $x/D =$ 15, where it is deflected to the right and then the left, respectively. This is illustrated schematically in Figure 3.7(c). The response of particles to such motions will depend on St_m. Smaller particles, those with $St_o \sim O(1)$, can be expected to be 'flung' radially outward by the large eddies in the regions between vortices as described by Longmire and Eaton (1992). This phenomena is clearly evident at $x/D \approx 15$ in Figure 3.7(a). Furthermore, differences in instantaneous jet spread may also be visually detected by comparing 3.7(a) and (b).

That particle distributions are preferentially concentrated along the centreline is also seen in the Figure 3.8, which presents the rms signal divided
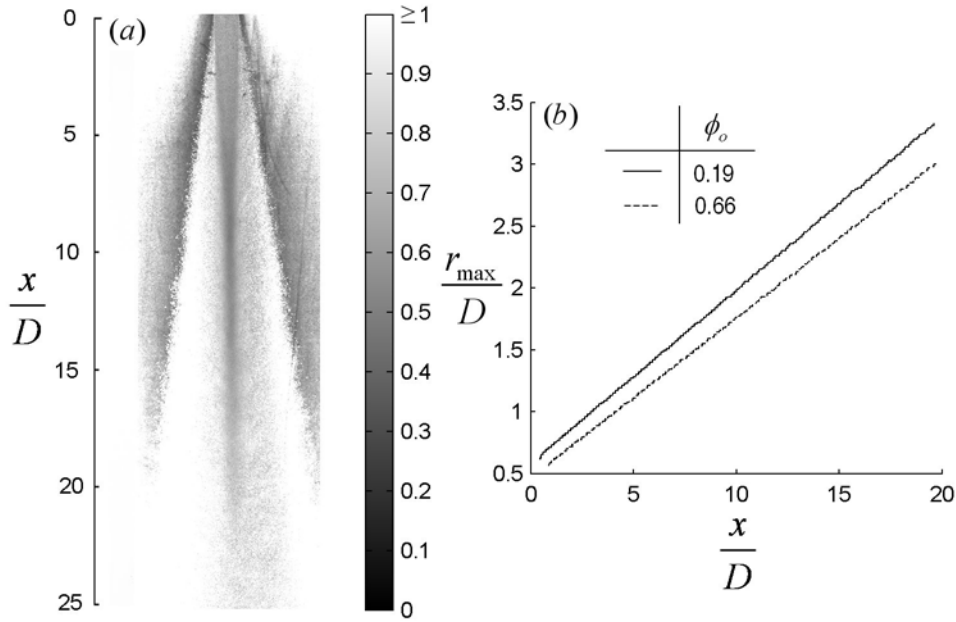
83

Figure 3.8: (a) Image of the locally normalised rms/mean signals for the case $\phi_o = 0.19$ and (b) line of best fit through the 'jet boundary', r_{max}, for two values of ϕ_o.

by the mean for the case $\phi_o = 0.19$. This method of presentation highlights both the maximum radial extent of the particles, r_{max}, and the core regions where particles are preferentially concentrated. The parameter r_{max} may be detected since the locally normalised rms/mean signal increases radially from the centreline, up to a maximum. The gray scale has been chosen so that all values greater than unity have been set to white. To avoid an undefined value for radial values beyond the jet, the background has been set to have a small positive value. In this way, the edge exhibits a relatively sharp cut-off with a well defined value. The locus of the maximum radial position at which particles are found, r_{max}, is found by a linear fit of this boundary. The result is plotted in Figure 3.8(b). The slopes for the cases $\phi_o = 0.19$ and 0.66 are found to be 0.140 and 0.129, respectively. Hence, the locus of r_{max} is also a function of ϕ_o. The case $\phi_o = 0.34$ is not presented due to the poorer signal to noise ratio.

The scaling factors developed in Chapter 2 for the gas phase velocity

84

and solid phase mass flux are assessed for the present particle distributions. Figure 3.9 presents the locus of $r_{1/2}$ and r_{max} scaled by the factor $x/D(1+\phi_o)^{-1/2}$. The collapse of data, relative to the unscaled data (Figure 3.5(a) and 3.8(b), respectively) is reasonable in both cases. Although an offset is evident in the scaling of r_{max}, both values of ϕ_o have the same slope of 0.166 (Figure 3.9b). While Figure 3.9 suggests $r_{1/2}$ scales with $x/D(1+\phi_o)^{-1/2}$, it is also plausible that $r_{1/2}$ may scale with $x/D(1+\phi_o)^{-1}$ as seen in Figure 3.9(c). However, the case $\phi_o = 0.66$ overshoots the other cases somewhat.

This ambiguity is deduced to be a result of the polydisperse distribution (Figure 3.1, Figure 3.6), the lack of wide variation in ϕ_o, and the non-linear nature of $r_{1/2}$. From Figure 3.6, it can be seen that particles span both the proposed regimes $St_o \lesssim 20$ and $20 \lesssim St_o \lesssim 200$ in Chapter 2, so that neither scaling regime can clearly prevail. Nevertheless, it is considered that the scaling of half widths with $x/D(1+\phi_o)^{-1/2}$ is appropriate. Not only is this because r_{max} scales well, but an inspection of the instantaneous images (Figure 3.7) and centreline distributions (Figure 3.5b) reveals that a large fraction of particles are only partly responsive. Hence, axial momentum exchange is considered to be important in addition to turbulence damping (see section 2.3.2). A greater range of ϕ_o would help to resolve this. Furthermore, because the half widths are non-linear, it is more difficult to judge whether data has collapsed.

3.3.1.2 The case, $St_o^* = 0.4$

The variation in ϕ_o is now considered for the case $St_o = 0.4$. Presented in Figure 3.10 is the mean image (a) for $\phi_o = 0.19$ and exit profiles (b) for all ϕ_o. Figure 3.10(b) shows that at the nozzle exit plane, the concentration of particles close to the pipe wall exceeds those at the centreline by approximately 50%. The preferential distribution of particles toward the wall has been detected previously for flows in the range $St_o^* < O(1)$ (Frishman *et al.*, 1997). As St_o^* approaches 1, the exit profile will approach a top hat shape as
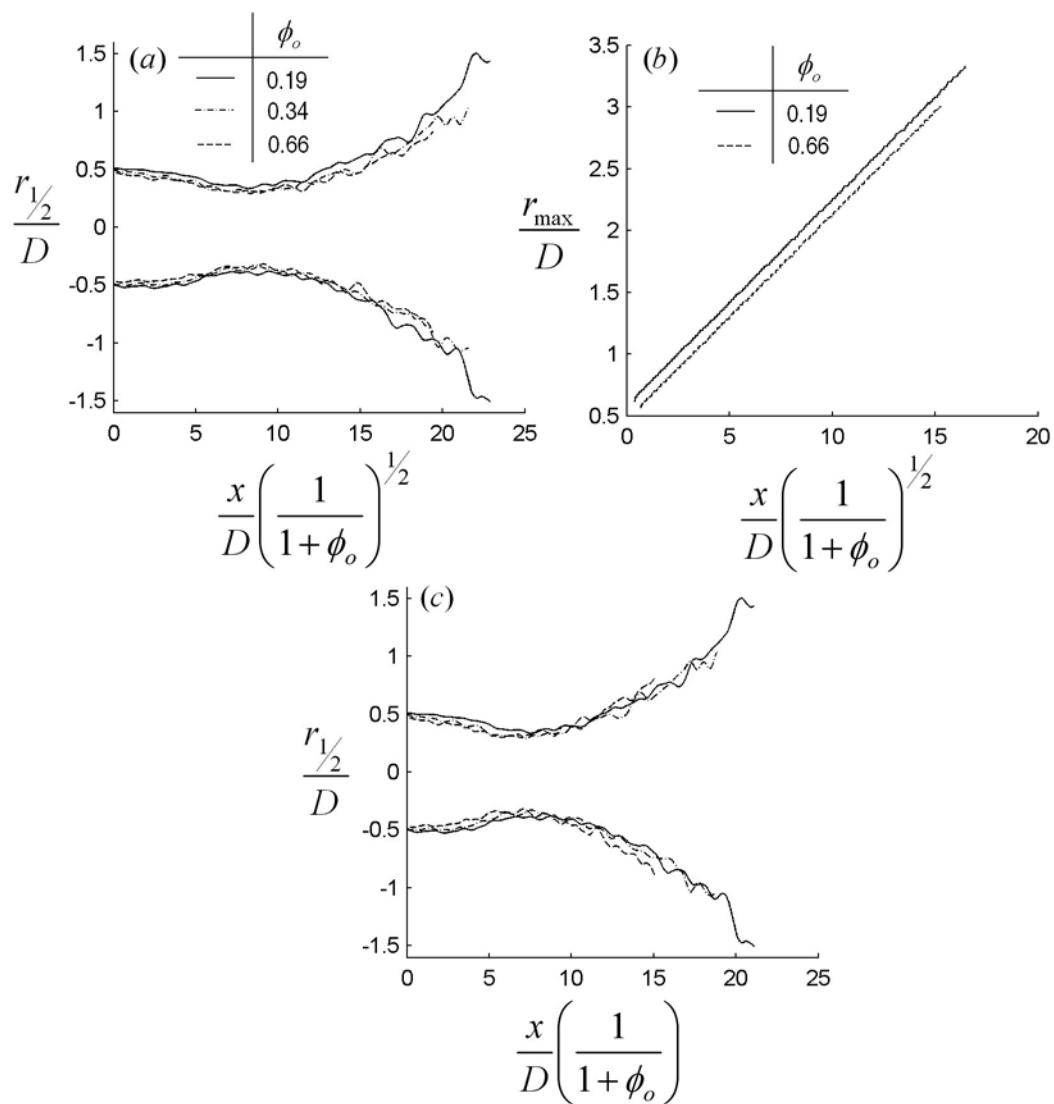
Figure 3.9: (a) Half widths and (b) jet widths scaled by $x/D(1+\phi_o)^{-1/2}$. (c) Half widths scaled by $x/D(1+\phi_o)^{-1}$.
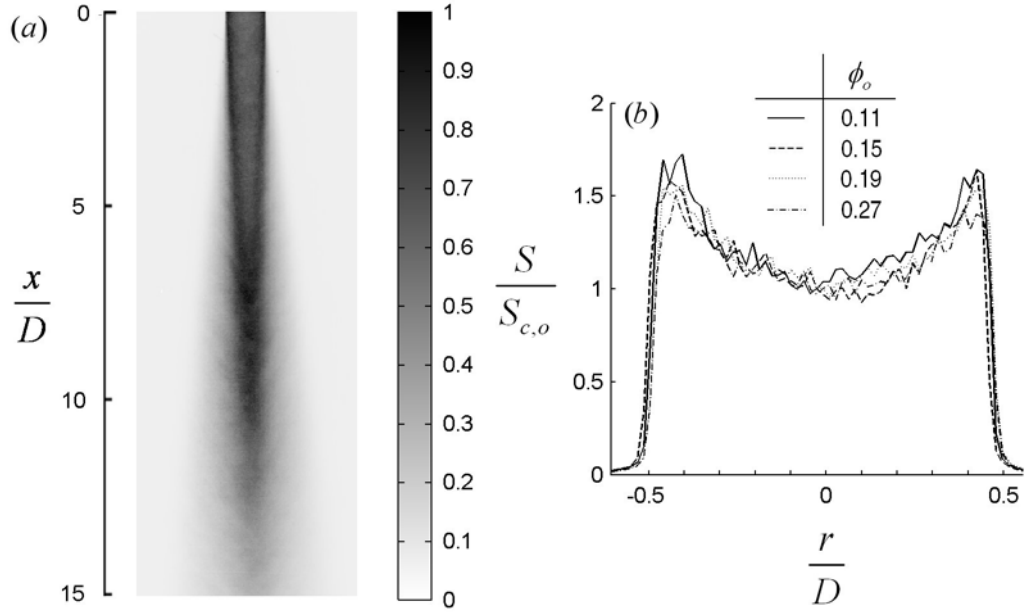
Figure 3.10: (a) Mean image of the case $\phi_o = 0.19$ and (b) exit profiles for all cases. $St_o = 0.4$.

detected above in Figure 3.3 for the case $St_o^* = 1$. The distribution of particles at the pipe wall and subsequently the jet edge, persists downstream until $x/D \approx 6$ as seen in Figure 3.10(a). Beyond that axial position, concentration peaks merge in the region of the 'pinch-effect'.

The location of maximum apparent centreline concentration according to Figure 3.11 occurs at $x/D \approx 7$, which is closer to the jet exit than the case $St_o^* \sim 1$ described above. Further contrasts with the case $St_o^* \sim 1$ are also evident in Figure 3.10. There is a clear dependence of $S_{c,o}$ on ϕ_o, yet an apparent independence of $r_{1/2}$ on ϕ_o. The quantity, r_{max}, also shows only a weak dependence on ϕ_o. These effects can be explained once more with reference to the cumulative particle size distribution at the axial location where $St_m = 1$ (Figure 3.11(d)). This Figure shows that by $x/D \approx 10$, essentially all particles are responsive to the decay of gas phase centreline velocity. Thus, it is found that the centreline distribution of particles are more readily dispersed for this case with respect to $St_o^* \sim 1$. However, because the particles are more responsive to the gas phase, there is less

damping of the jet turbulence since the gas phase will expend less work accelerating the particles. Hence, large scale jet mixing with the ambient fluid and the corresponding expansion of the gas phase shows only a weak dependence on ϕ_o.

The responsive nature of the particles may also explain the dependence of $S_{c,o}$ on ϕ_o. In this case, particles act to increase the density of the jet and hence, the decay rate of the centreline velocity could be expected to be reduced. Correspondingly, the dispersion of particles is reduced with increasing ϕ_o. These issues will be discussed further in section 3.3.3 below, where the gas phase jet exit density is varied.

3.3.2   The variation of St_o^*

In this section, the effects of a variation of St_o^* on particle distributions is addressed. It is evident from the exit profiles presented already in Figures 3.3 and 3.10, that for low St_o^*, the profiles assume a concave shape which, as St_o^* increases, tends toward a flatter profile for $St_o^* = 1$. From Figure 3.12(b), it can be seen that the exit profile for the case $St_o^* = 3$ is of a convex shape, with the maximum signal occurring at the centreline, a value that is 40% greater there than at the jet edges. The presence of the pinch-effect may also be observed in the mean image of Figure 3.12(a), as it has been seen in both the other mean images prior to this.

The dependence of the pinch-effect, or position of maximum centreline concentration, x_p on ϕ_o and St_o^* is shown in Figure 3.13(a) and (b), respectively. The results of Figure 3.13 imply that x_p is approximately independent of ϕ_o, at least for the range of ϕ_o tested. However, one may note the large amount of scatter in these results. The cause of this is the inherently noisy images. Although filtering the data has helped reduced the noise significantly, there is still a degree of fluctuation between cases of similar ϕ_o. The scatter of data is also evident in Figure 3.13(b). However, it can be deduced from this figure, and the previous result of Laats and Frishman (1970) and
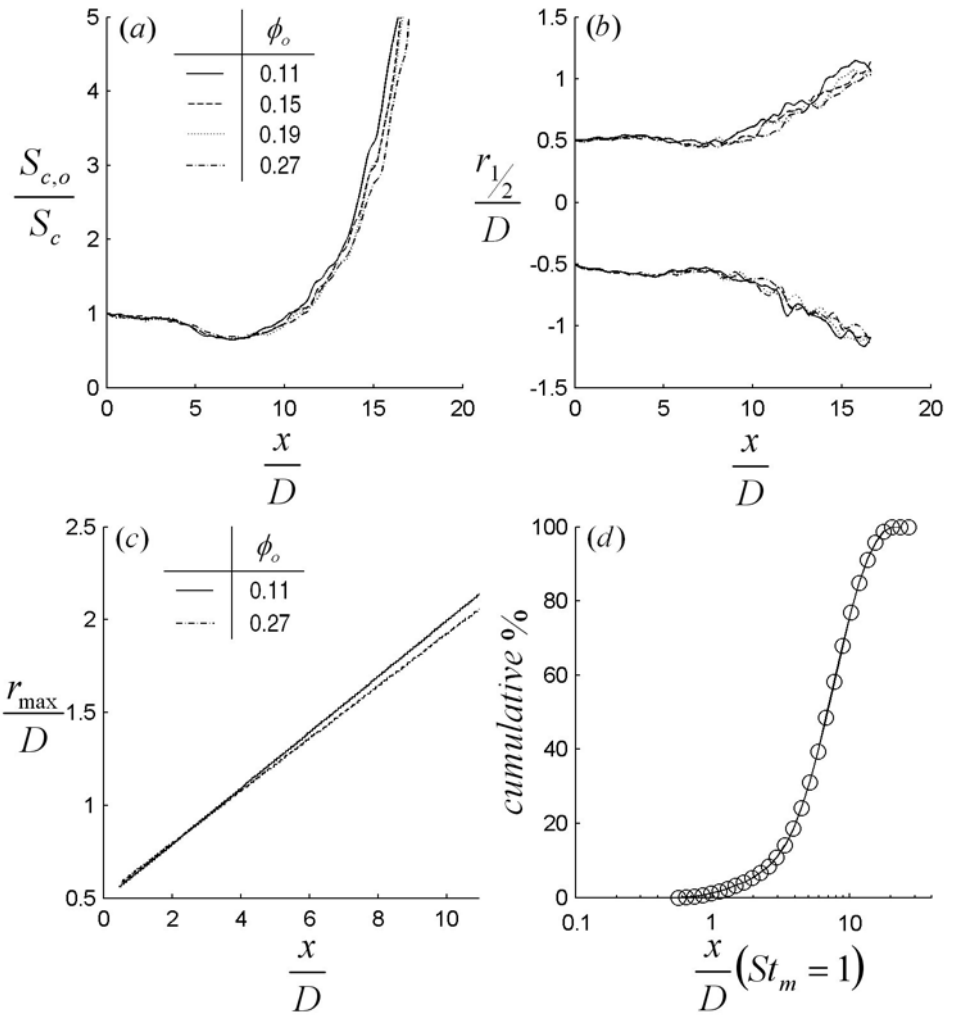
88

Figure 3.11: (a) Centreline values, (b) Half widths, (c) Loci of maximum particle dispersion and (d) cumulative size distribution indicating the axial distances at which $St_m = 1$.
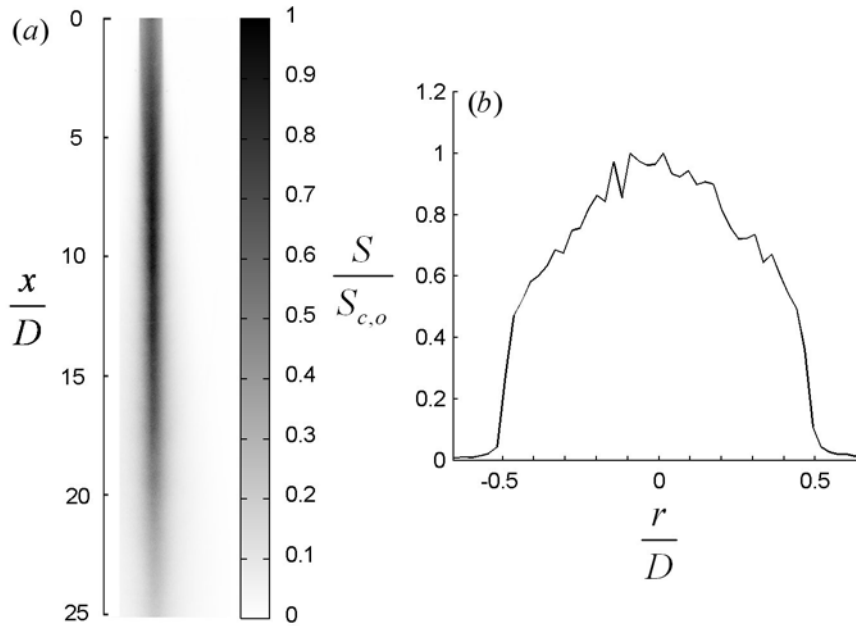
Figure 3.12: a) Mean image and (b) its exit profiles for the case $St_o^* = 3$, ϕ_o = 0.71.

Frishman *et al.* (1997) that the dependence of x_p on St_o^* causes x_p to be displaced downstream as St_o^* is increased.

It is noted that there is a quantitative difference between these measurements and those of Laats and Frishman (1970) and Frishman *et al.* (1997). Firstly, the magnitude of the increase in concentration detected here (see Figure 3.14) is greater than in measurements by LDA (Frishman *et al.*, 1997) and isokinetic sampling (Laats and Frishman, 1970) by approximately 25% and 35%, respectively. Secondly, the location of the pinch effect is closer to the origin here (see Figure 3.13(a)) by almost a factor of 2 compared with Frishman *et al.* (1997), while they are roughly equal with respect to measurements by Laats and Frishman (1970). This however, is dependent on St_o as Figure 3.13(b) indicates.

The dependence of both the centreline decay and half width on St_o^* are displayed in Figure 3.14(a) and (b), respectively. Consistent with the discussion above and in the previous chapters, the decay of the apparent centreline
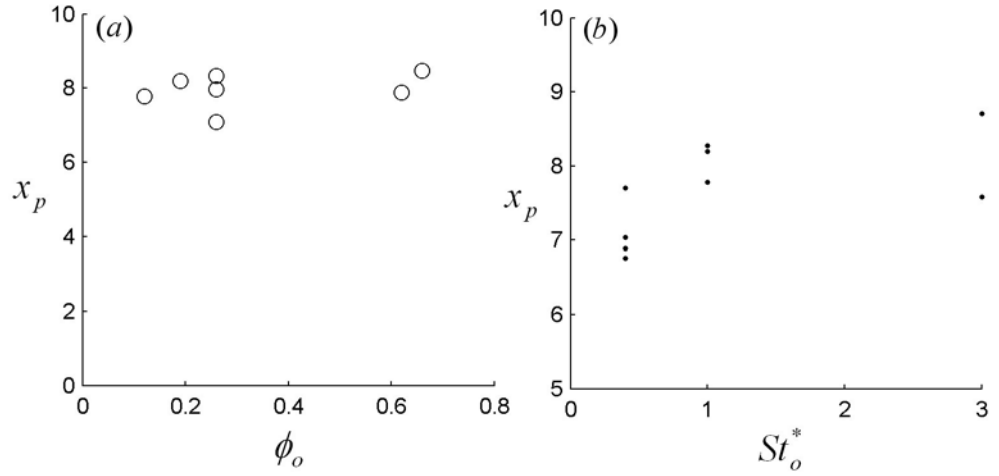
Figure 3.13: The dependence of the location of the pinch-effect, x_p, on (a) ϕ_o and (b) St_o^*.

concentration, as well as the spread of particles, is reduced as St_o^* is increased. As the inertia of particles increases, they are less able to respond to the large scale turbulent motions, those most responsible for their dispersion. Hence, a greater fraction of particles will be distributed toward the jet centreline as St_o^* is increased.

3.3.3 The variation of ρ_j/ρ_a

The centreline decay and half width for the variable density case ($\phi_o = 0.62^h$) is displayed in Figure 3.15 in comparison with the case $\phi_o = 0.66$. It can be seen that the centreline decay rate for the 'hot' case is slightly less than for the 'cold' case. This can be explained by the greater centreline velocity decay rate in a hot jet than in a cold one. Rewriting St_m in terms of a constant K leads to

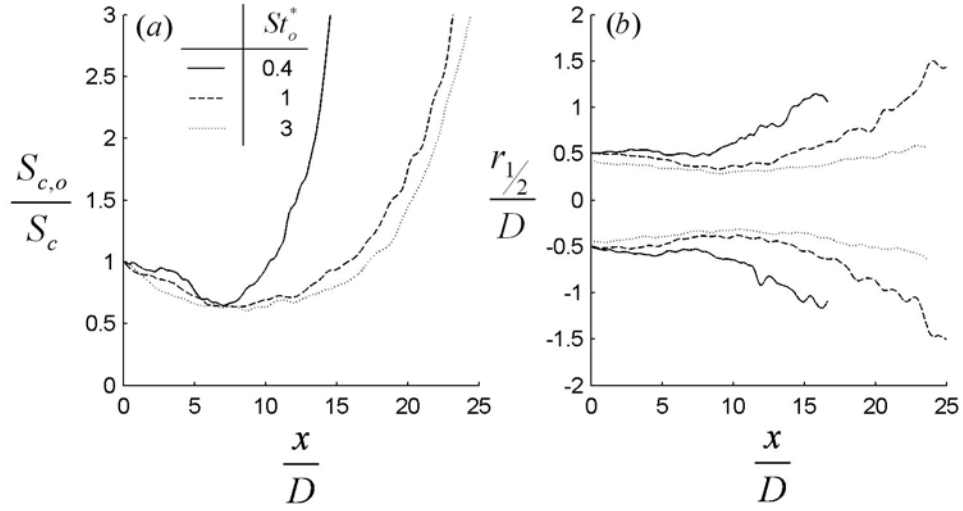$$St_m = \frac{St_o}{K} \left(\frac{D}{x}\right)^2.$$

(3.5)

91

Figure 3.14: (a) Centrelines and (b) half widths for a variation in St_o^*. For $St_o^* = 0.4$ & 1, $\phi_o = 0.19$ and for $St_o^* = 3$, $\phi_o = 0.71$.

However, for a variable density jet, K is modified by the density ratio (Chen & Rodi, 1980) so that

$$K = K_1 \left(\frac{\rho_j}{\rho_a}\right)^{1/2} \qquad (3.6)$$

where K_1 is the centreline decay constant. Substituting this into equation 3.5 leads to

$$St_m = \frac{St_o}{K_1} \left(\frac{\rho_a}{\rho_j}\right)^{1/2} \left(\frac{D}{x}\right)^2, \qquad (3.7)$$

which shows that St_m increases as the jet density is reduced. Equations 3.4 and 3.7 are also presented in Figure 3.15(a), which show the small increase in St_m corresponds to the small decrease in the decay rate of the case $\phi_o = 0.62^h$ with respect to the case $\phi_o = 0.66$. In contrast, no dependence of spread on the density ratio is detected (Figure 3.15b). This is expected since the gas phase velocity will not exhibit a dependence of spread on ϕ_j/ϕ_a itself (Chen & Rodi, 1980). That is, while the range of density variation is small, the results are consistent with equation 3.7. Further work is required to extend this to a greater range of density ratios.
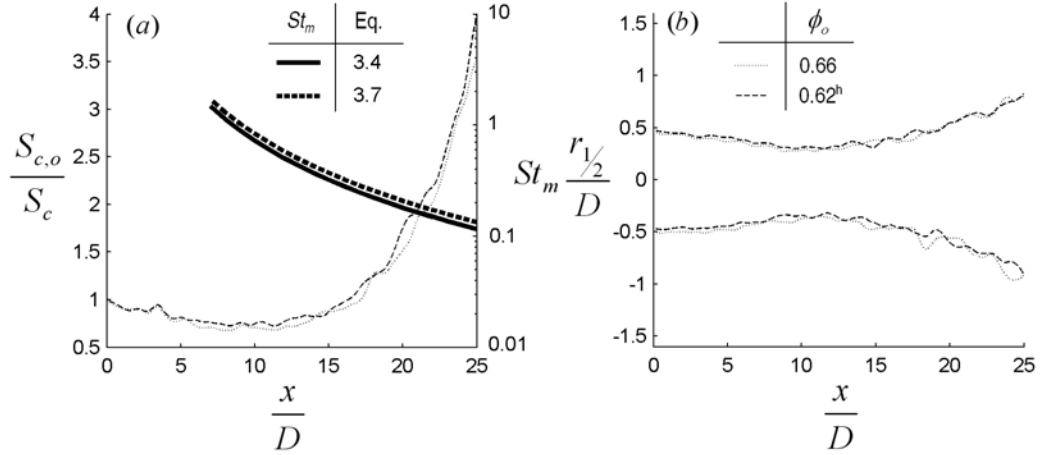
Figure 3.15: (a) Centreline values and (b) half widths for the case $\phi_o = 0.66$ and the 'hot' jet $\phi_o = 0.62^h$.

3.4 Conclusions

In this Chapter, measurements of particle-distributions in an axisymmetric turbulent jet for a variation in ϕ_o, St_o^* and ρ_j/ρ_a were presented. For $St_o^* \sim 1$, the distribution half widths, although somewhat ambiguous, were found to scale with $x/D(1 + \phi_o)^{-1/2}$. The ambiguity is attributed to the polydisperse size distribution, non-linearity of the half-widths and the limited range of ϕ_o. In contrast to the half widths, the centreline velocity was found to be independent on ϕ_o. This is attributed to the polydisperse particle size distribution, since a large fraction of the particles remain distributed on the centreline, unresponsive to the gas phase. For $St_o^* < 1$, the half width was found to be independent of ϕ_o, while a centreline dependence was detected. The independence of the half width is consistent with the hypothesis that there is negligible turbulence modulation due to a sufficient proportion of the particles being sufficiently responsive to the large scale eddies.

The exit profiles were also inspected for a variation in the exit Stokes number based on friction velocity, St_o^*. Consistent with the results of Frishman *et al.* (1997), for $St_o^* < 1$, a concave exit profile was detected while for $St_o^* > 1$, a convex profile was detected. A flat profile was detected for

93

$St_o^* \sim 1$. The decay of apparent centreline concentration and half widths are reduced for an increase in St_o^*. The location of the pinch-effect, x_p was found approximately independent of ϕ_o, however, a large scatter in the data was evident. It was found however that x_p was displaced further from the origin as St_o^* increases, consistent with Frishman *et al.* (1997).

The variation of jet density ratio was assessed but limited conclusions can be drawn from this because of the small difference in density ratio for the 'hot' jet compared with the ambient case. Nevertheless, a slight dependence of the apparent centreline concentration is detected with ρ_j/ρ_a. This is consistent with the small increase in jet time-scale and hence St_o^* with ρ_j/ρ_a so that particles are slightly less responsive to the gas phase.

Chapter 4

Mean particle distributions in a two phase triangular oscillating jet flow

4.1 Introduction

Many experimental studies of particle-laden jets have been undertaken with relatively simple axisymmetric configurations (e.g. Laats and Frishman, 1970, Elghobashi *et al.*, 1984, Hardalupas *et al.*, 1989, and Sheen *et al.*, 1994) as detailed in Chapter 2. However, most practical burners use more complex devices, such as annular nozzles, swirl and/or highly unsteady jets and there is less data available for such flows. Particle-laden flows though devices such as these have been investigated by Borée *et al.* (2001), Wicker and Eaton (2001) and Morris *et al.* (1992), respectively. Particle distributions from the highly unsteady triangular oscillating jet of Lee *et al.* (2003), with potential application in pulverised fuel combustion, are yet to be reported.

Highly unsteady jets are more complex than simple axisymmetric ones and, perhaps as a consequence of this, very few particle-laden studies of

such flows have been reported. In this context it is noted that all turbulent jets are unsteady. The term 'highly unsteady' is employed here to denote large scale oscillations in the underlying flow, such as the precessing vortex core of swirling flows (Syred, 2006) and precessing jet (PJ) flows (Nathan *et al.*, 2006). The measurements of Morris *et al.* (1992) are an important exception. They studied a particle-laden, fluidically oscillated slot jet and found the initial spread, and hence entrainment in this jet, to be greater than that from the corresponding steady slot jet.

In a series of studies on the effect of precessing round jets on particle-laden flows, Smith *et al.* (1998a,b) showed that this highly unsteady flow can also increase the initial spread of particles compared with steady flows. They also demonstrated that the PJ offers some favourable combustion characteristics, such as an increased particle burn-out, a five-fold reduction in ignition distance and the potential for reduced NO_x emissions. Smith *et al.* (2000) also showed an increased particle clustering and deduced that these effects can be beneficial. Nathan and Hill (2002) further showed that PJ flows can be beneficial in full-scale cement kilns. As a consequence of the promising nature of these trials, preliminary measurements of particle distributions in a PJ flow were conducted (Birzer *et al.*, 2005) at laboratory scale to further the understanding of particle-laden PJ flows. In that study, a method similar to that used here, yielded centreline particle distributions and half widths. The primary aim of the present study is to compare these data of Birzer *et al.* (2005) with the distribution of particles from a triangular oscillating jet nozzle.

The triangular oscillating jet nozzle of Lee *et al.* (2003) generates a highly unsteady flow that is closely related to that of the PJ nozzle. It has been devised to produce a lower pressure-drop than the PJ in order to enhance its applicability to particle-laden industrial flows. The first description of this device is in the patent of Mi *et al.* (1999). The triangular oscillating jet (OJ) nozzle is shown schematically in Figure 4.1. The OJ nozzle comprises a cylindrical chamber with a triangular orifice at its inlet, and a circular lip at its outlet. Lee *et al.* (2003) have shown that this nozzle, with suitable geo-

Figure 4.1: The configuration of an oscillating triangular jet nozzle showing the triangular inlet, the cylindrical chamber and the lip (Top). The flow through the chamber exhibits an asymmetrical reattachment and oscillates with time. The probability distribution of the emerging jet shows that the jet exhibits a 3 lobed cross-section (Bottom) as measured by Lee et al. (2003).

metric ratios, produces a jet which instantaneously emerges from the nozzle at a significant angle to the x-axis (see Figure 4.1) and oscillates to produce, on average, rapid initial spreading.

Unlike the round inlet of the orifice of the precessing jet nozzle, the three corners of the triangular inlet orifice result in preferential attachment within the chamber, which consequently produces a three-lobed distribution of the time-averaged emerging jet (Figure 4.1). Further, the loss in kinetic energy through an OJ nozzle is approximately 5 times less than that of a PJ nozzle (Lee et al., 2003). Hence, in contrast to a PJ nozzle, the flow from an OJ nozzle requires less pressure to drive it. For this reason, the OJ nozzle is potentially more suited to industrial applications involving pulverised fuel where higher pressures usually translate into higher operating and capital costs (e.g. larger fans or blowers). However, at the same time, the spreading

rate of the OJ nozzle is less than that from the PJ. Hence, investigations are required to determine the range of conditions under which each offers an advantage.

For these reasons, the aims of the work in this chapter are i) to determine the effect of the momentum ratio of an OJ flow to that of a particle-laden annular stream on distributions of particles, ii) to determine the influence of the exit mass loading on these distributions and iii) to compare the distributions with those in a particle-laden PJ flow.

4.2   Experimental details

A planar light scattering technique similar to that in Chapter 3 was employed to measure mean particle distributions in a particle-laden triangular oscillating jet flow. Measurements of particle distributions are chosen ahead of velocity, both because of its direct relevance to combustion applications and because it also avoids the need to address out of plane motions (Wong *et al.*, 2003). It also allows larger image regions for the same effective resolution relative to Particle Image Velocimetry due to the need to correlate velocity from a box of multiple pixels. Eaton *et al.* (1996), Roquemore *et al.* (1986) and many others have shown that planar light scattering techniques are well suited for use in more complex flows, such as those with large scale structures and/or are highly unsteady.

4.2.1   The triangular OJ Nozzle

Shown in Figure 4.2 are the main features of the two phase, oscillating jet nozzle. The inlet diameter to the orifice (D_o) and chamber diameter (D) are equal to 51mm and 50mm, respectively. The exit lip (d_2) has a diameter of 40mm. The orifice is an equilateral triangle with each side of length 19.2mm, and an equivalent diameter (d_e) of 14.3mm based on a circular nozzle of equal

Figure 4.2: Schematic diagram of the key components of the OJ nozzle (adapted from Lee et al., 2003).

area. The expansion ratio, defined as the ratio of the chamber diameter to the equivalent orifice diameter (D/d_e), is thus equal to 3.5. These dimensions ensure optimal jet spread based on the measurements of Lee et al. (2003). The orifice is located 122mm upstream from the exit plane so that L/D = 2.44.

4.2.2 The annular section

Also shown in Figure 4.2 is the annular channel through which particles are conveyed. This channel has an outside diameter (D_n) of 60mm, while the inside diameter of the annulus (D_A) is 70mm. The injection of particles into the annulus occurs approximately 2m upstream from the exit plane. Previous measurements show that a single radial inlet to this upstream inlet position results in a significant asymmetric particle distribution at its exit plane (Birzer et al., 2005). In response, a number of alternative inlet configurations were tested, such as tangential inlets, dual and quadruple radial inlets as well as 'slot' inlets. Of these, the best performing was the dual opposing radial inlets. Hence this configuration is used here (shown later in Figure 4.4).[1]

----
[1]For reference: the particle distributions from the tangential inlet was found to be considerably more biased than a single radial inlet, most likely due to the lack of development length. The quadruple radial inlets are vulnerable to the difficulty of splitting the

4.2.3 Experimental conditions

The velocity of the annular section, U_2 was held constant at 28m/s, while that through the OJ was varied. To estimate the exit velocity of the OJ requires knowledge of the percentage of nozzle exit area occupied by the partially confined oscillating jet. For the PJ nozzle, Wong *et al.* (2005) has measured the phase averaged exit flow field. These measurements estimated the exit area occupied by the instantaneous emerging jet to be as one third the total exit area. Unfortunately, detailed measurements of the phase averaged OJ are not available. However, measurements have been performed for a closely related configuration in which the jet remains attached to a fixed location (Lee *et al.*, 2004). From this data, we can estimate the proportion of the nozzle exit plane occupied by the jet to be approximately 40% of the exit area. This is then used to estimate the bulk exit velocity for the cases presented below as 25, 38, 77 and 99m/s. The corresponding momentum ratios, G_1/G_2, are 0, 0.4, 0.9, 3.7 and 6.1. Here, G_1 is the bulk mean momentum of the flow through the instantaneous exit plane of the OJ or PJ nozzle and G_2 is the bulk mean momentum of the gas phase alone through the annulus. The exit mass loading is held nominally constant at approximately $\phi_o = 0.12$ and is defined to be

$$\phi_o = \frac{\dot{m}_p}{\dot{m}_2}, \tag{4.1}$$

where $\dot{m}_p$ is the solid phase mass flow rate and $\dot{m}_2$ is the fluid mass flow rate through the annulus. The mass loading is varied from between 0.08-0.36 and 0.09-0.51 for the cases $G_1/G_2 = 0$ and 6.1, respectively.

The present values of G_1/G_2 span the same range as those investigated for the PJ nozzle by Birzer *et al.* (2005), $G_1/G_2 = 0$, 0.22, 0.75, 1.8 & 6.3 for $\phi_o = 0.15$. The PJ experimental conditions were conducted in the same facility. However, Birzer *et al.* (2005) used $U_2 = 18$m/s. In addition to this, while the PJ nozzle dimensions D_A and D_n are the same, Birzer *et al.* (2005) also used a smooth contraction to the circular inlet orifice

---

flow equally, a well known problem even for single phase flows. The slots, although they performed well in smaller scale tests, did not do so at this scale.
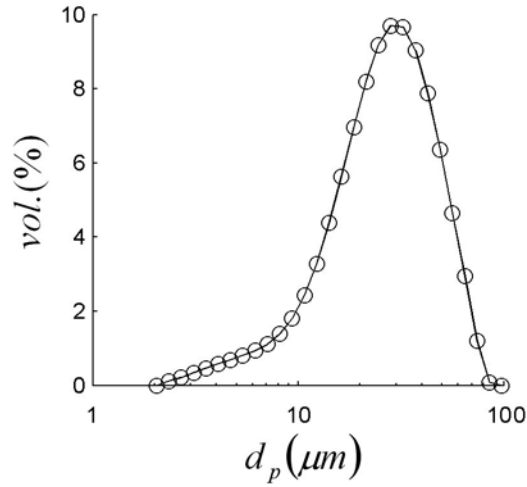
Figure 4.3: Qcel 5070s particle size distribution.

and a bluff body positioned slightly upstream from the exit plane. The particles used in both experiments were the commercially available Qcel 5070s hollow glass spheres with a density of 700kg/m^3 from Potters Industries Inc. The particle size distribution, measured with a Malvern Mastersizer 2000, is displayed in Figure 4.3. The volume weighted mean diameter (d_{43}) is 29.2μm. The particle type is chosen both to simulate the polydispersed particle size distribution usually found in industrial flows and also to maintain exit Stokes number similarity with typical full scale approximations in a cement kiln. The exit Stokes number is defined here as

$$St_o = \frac{\tau_p}{\tau_g} = \frac{\rho_p d_p^2 U_2}{18\mu D_n}. \tag{4.2}$$

This gives a mean exit Stokes number, based on d_{43} of $St_o = 0.9$. However, the dominant time scale in an oscillating jet is at least an order of magnitude larger than that from a simple jet (Nathan *et al.*, 1998), so that the characteristic Stokes number is expected to be an order of magnitude lower than that suggested by equation 4.2. Also, the largest particles have Stokes numbers an order of magnitude higher, and the smallest particles an order of magnitude smaller than this value, an issue discussed in more detail below.

101

4.2.4 Apparatus

Shown in Figure 4.4 is the experimental apparatus, including key features of the particle delivery and flow development systems. Regulated compressed air feeds all lines including the fluidised bed particle feeder. The fluidised bed is mounted on a fulcrum and placed over a load cell for measurement of the particle mass flow rate, $\dot{m}_p$, which is linear with time to within 0.3% (based on the linear correlation coefficient) for the worst case. A reference weight of 100g was used to calibrate the system. Particles were drawn from the fluidised bed into the annulus line via a venturi. The flow was split using a tee section and delivered to the vertical pipes via opposite radial inlets. The lengths of the vertical pipes preceding the annulus and OJ nozzle were approximately 2m. This corresponds to $L/D = 55$ & $L/a = 400$, where $a = D_a - D_n$ (Figure 4.2) is the distance between the inside diameter of the annulus and outside diameter of the OJ nozzle. Earthed wires were attached to the pipes to discharge any static electricity. The annular pipes were aligned on the axis of a square working section of an open loop wind tunnel of 650mm sides. Flow conditioning of the co-flowing air comprises five consecutive screens, straws and a bell mouth, used to reduce swirl and background turbulence within the working section. An induced draught fan provides the motive force for the tunnel and delivers the particle-laden flow to a bank of cyclones. To simulate a cement kiln environment and match the conditions of Birzer *et al.* (2005), a co-flow velocity of approximately 8.0 ± 0.3m/s was chosen (Birzer *et al.* 2007).

The supply or driving pressure, P_d, presented below, has been measured separately from those measurements where a particle-laden annular stream is present. A pressure gauge upstream from the nozzle gives a pressure reading, while the pressure drop between the gauge and the nozzle was estimated and subtracted from the measured value.
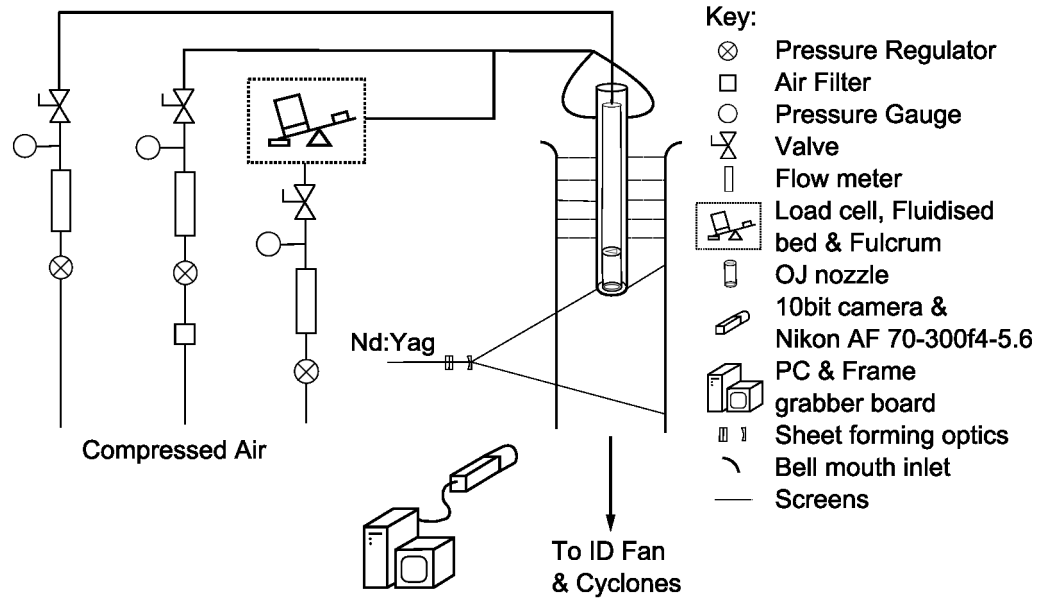
Figure 4.4: Experimental arrangement.

4.2.5 Optics

The intensity of the scattered light is proportional to the square of the diameter of particles (see Chapter 1) within a given pixel volume. The measured signal is thus of some direct interest since it is both proportional to the particle surface and cross-sectional area. It is also indicative of particle concentration. However, since the size distribution of particles is broad (Figure 4.3), it is impossible to convert the signal to number density (or mass density) without a reference measurement or without employing additional assumptions, such as a constant size distribution throughout the flow. In previous planar light scattering techniques, investigators (Ferrand *et al.*, 2001, 2003) have determined the local mass concentration via droplet fluorescence in a polydispersed two phase, axisymmetric nozzle flow. However, particles coated with fluorescent material are notoriously expensive and the coating is vulnerable to abrasion. Further, the simultaneous measurement of fluorescence and scattering can only be used to measure mean particle
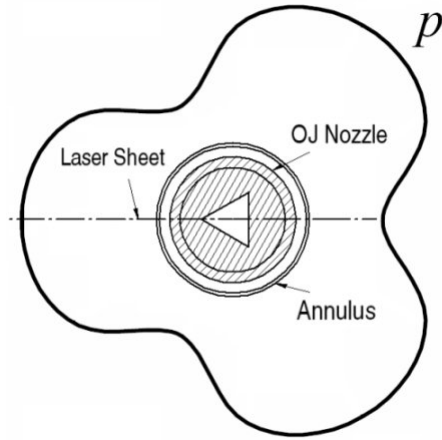
103

Figure 4.5: Location of Laser sheet relative to the OJ nozzle and its azimuthal probability distribution function, p first described in Figure 4.1.

size distribution and not on a shot by shot basis, unless the particle size distribution is very narrow. This is because the cubic dependence of fluorescence signal on particle diameter means that particles with only one order of magnitude difference in size have three orders of magnitude stronger signal. Hence, this approach has a very small dynamic range and would not be suitable for our size distribution. For these reasons, the current planar scattering technique was chosen.

Details of the light sheet forming and collection optics are also shown in Figure 4.4. An Nd:Yag, 10Hz pulsed, 532nm Quantel laser was used to produce a sheet of approximately 0.5mm thickness, aligned with a corner of the triangular orifice, as shown in Figure 4.5. Also shown in Figure 4.5 is the relative position of the azimuthal probability distribution function of the emerging jet as found by Lee *et al.* (2003) and previously shown in Figure 4.1. An area of approximately 500mm × 500mm was imaged with a NIKON AF 70-300mm f4-5.6 zoom lens onto a 10bit CCD array of 1008 × 1018 pixels to provide a spatial resolution of approximately 0.5mm in each direction. To avoid pixel saturation, f-stops of 8 and 11 were mostly used depending on the mass loading, although in one high loading case, an f-stop of 16 was used.

4.2.6   Post-processing

For each set of operating conditions, 200 instantaneous images were saved on a frame grabber board. Each image was then corrected for variations in laser sheet profile, camera gain, collection optics and CCD noise (electronic plus background). Correction images were obtained by filling the working section with smoke and illuminating with laser light at the same power to that of the experiments. To compensate for the weaker scattering of the smoke, a lower f-stop of 4 was used to record 200 smoke images. Differences in imaged spatial intensity occur with different f-stops, especially at the image edges due varying degrees of diffraction through the camera lens. These differences were assessed using measurements of a blank sheet with different f-stops, and found to be approximately 3% at worst at the image edges between f-stops of 4 and 16. No attempt was made to correct for this since such corrections may be counter-productive due to imperfect blank sheet illumination. A background correction was made by subtracting a mean background image. Pixel saturation was assessed by finding the percentage of pixels on the jet centreline that are saturated. This was found to be less than 0.2% for the highest loading which is within measurement uncertainties. The mean images were found to be noisy, probably due to marker shot noise (Long *et al.*, 1981). A 2 pass, 20 pixel moving average filter applied to centreline data and half widths presented below was found to remove much of the noise, but at the expense of reduced spatial resolution.

4.2.7   Sources of error

Despite some considerable effort, some misalignment and flow bias was found in the two phase annular flow. Figure 4.6 shows the mean exit profile of the scattered signal, S, from the emerging flow. Also presented are the profile 'widths' at approximately half the peak signal. On the left, the side through which the laser beam enters the flow, denoted the 'strong side', the width is approximately 12 pixels, while on the right, 'the weak side', it is 10 pixels.
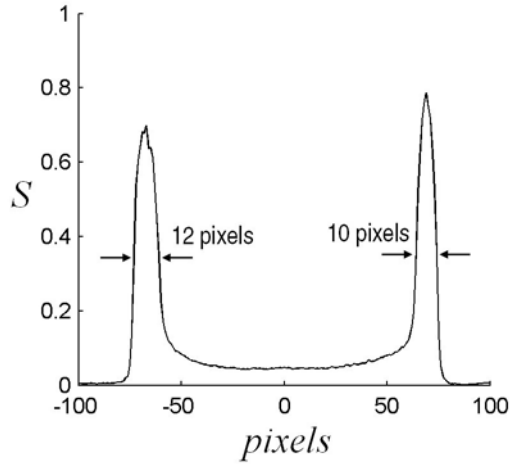
Figure 4.6: Exit profile for $G_1/G_2 = 0$ showing resolution and width of annular streams of particles.

Because the pixel resolution is estimated to be approximately 0.5mm, the eccentricity is estimated to be about 1mm, corresponding to an approximately 20% eccentricity of the nozzle.

Due to this asymmetry, the flow converges to a 'jet centreline' which does not necessarily correspond to the centre of the nozzle. The apparent jet centreline is defined as the radial position where the locus of maximum signal, r_{max}, converges noting that this may also vary to within 10% between each run. The locus of maximum signal is presented in Figure 4.7(a) for the case $G_1/G_2 = 0$, $\phi_o = 0.12$. From this figure, it is evident that the annular flow converges to the axis at $x/Dn \approx 3$. Within the first 3 diameters, r_{max} is almost exclusively identified in the annular flow on the strong side, the cause of which is attributed to attenuation of the light sheet in the near field. For the range $x/D_n > 3$, attenuation is deduced to be less significant (see below). The convergence of r_{max} (Figure 4.7a) is obtained with a line of best fit, as shown in Figure 4.7(b) for the range $x/D_n > 4$. This shows that the locus of maximum signal is found to converge to approximately $r/D_n = $ -0.15, i.e. on the laser side of the nozzle centreline. Evidence presented below suggests that this is not primarily a consequence of light sheet attenuation.
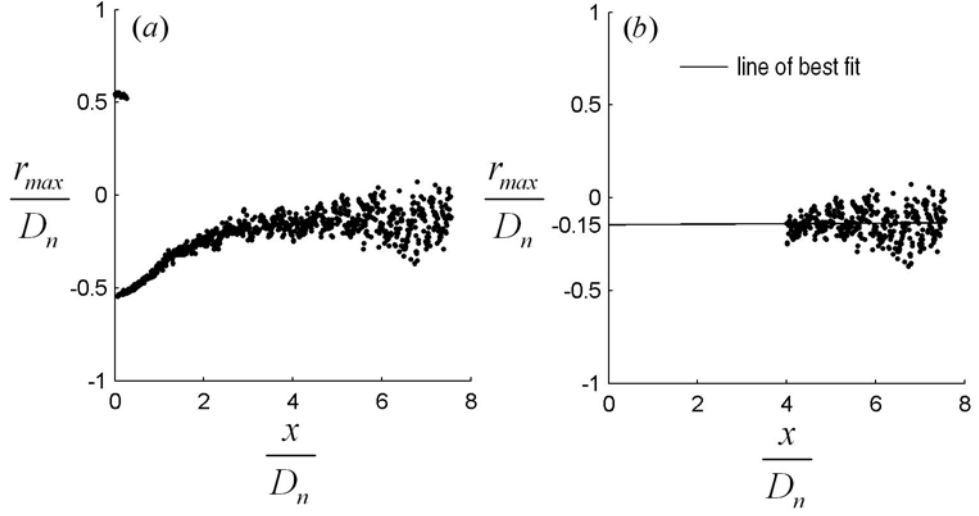
106

Figure 4.7: Locus of the points of maximum signal, r_{max}/D_n (a) for radial profiles, $G_1/G_2 = 0$, $\phi_o = 0.12$ and (b) the line of best fit of data in the range $x/D_n > 4$ used to identify the approximate adjusted flow centreline.

To quantify the effects of light sheet attenuation, the symmetry of radial profiles are assessed by calculating, $\Delta r_{1/2}$, which is the difference in half width from the strong side compared with the weak side, i.e.

$$\Delta r_{1/2} = \left(\frac{r'_{1/2,s} - r'_{1/2,w}}{r'_{1/2,s}} \right) \tag{4.3}$$

over the range $3 < x/D_n < 6$. Here, $r'_{1/2,s}$ and $r'_{1/2,w}$ are the strong and weak side half widths calculated with respect to $r/D_n = $ -0.15, respectively. The assessment is performed for the case $G_1/G_2 = 0$ for the following reason. The light sheet thickness is approximately constant, while the total jet spread changes with axial distance and with nozzle operating parameters. Hence, the proportion of particles within the light sheet, and the total amount of attenuation, decreases with increased spread of the jet. Thus, attenuation is most significant for the case $G_1/G_2 = 0$, where the jet spread is found to be least.
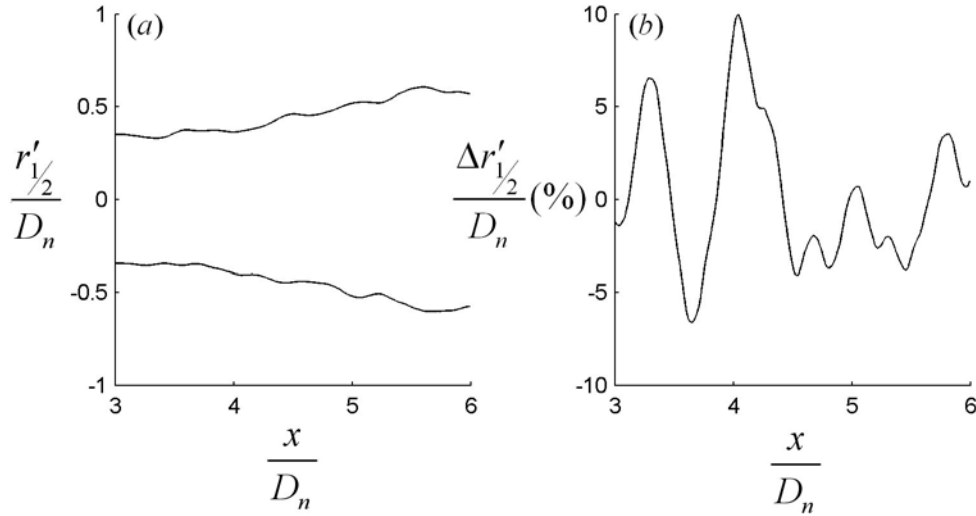
Figure 4.8: (a) Half widths taken with respect to the adjusted centreline, $r/D_n = $ -0.15 and (b) $\Delta r_{1/2}$ calculated according to equation 4.3 for the case $G_1/G_2 = 0$, $\phi_o = 0.12$.

Figure 4.8(a) presents the half widths (filtered) on the strong and weak sides based on the converged centreline, $r/D_n = $ -0.15. The values of $\Delta r_{1/2}(\%)$ are displayed in Figure 4.8(b). It can be seen that $\Delta r_{1/2}$ has a mean value of 0.3%, but with a large standard deviation of 4%. The data identifies a large-scale oscillation in the jet width with a pitch of about one nozzle diameter. The oscillations appear to be a consequence of marker shot noise, which is expected to generate a random scatter of raw data. Importantly though, the very low mean value of $\Delta r_{1/2} = 0.3\%$ reveals a high degree of symmetry, which implies that the effects of attenuation on the mean flow are small for the case $G_1/G_2 = 0$, in the range $x/D_n > 3$. Furthermore, based on arguments presented above, the effects of attenuation can be expected to be reduced with increased jet spread, i.e. with increased G_1/G_2. The influence of ϕ_o on attenuation is discussed below.

4.3 Results

4.3.1 Mean images & Exit Profiles

Mean images of particle distributions, averaged from 200 instantaneous images, are presented in Figure 4.9 for five values of G_1/G_2 at a nominal exit mass loading, $\phi_o = 0.12$. Inspection of Figure 4.9 shows clearly that the spread and decay rate of the particles increases as G_1/G_2 is increased. This demonstrates that the OJ flow is effective in increasing the spread of particles. The case $G_1/G_2 = 0$ effectively corresponds to a bluff body flow in which an annular counter rotating vortex (see the annular momentum dominated case of Roquemore *et al.*, 1986), is generated upstream from the point of convergence of the mean flow. A central recirculation zone (CRZ), generated either by a bluff body or swirl, is well known to tend to enhance flame stability and increase overall flow stability (Beer & Chigier, 1974). However, the size of the CRZ in the flow from the present nozzle is small. Hence, based on the findings of Smith *et al.* (1998a,b) for an annular PJ arrangement, the small central recirculation region can be expected to have little influence on a pulverised fuel flame compared with the OJ flow.

Local instantaneous recirculation is also present in an OJ flow, generated by the entrainment into the chamber by the partially confined jet (Lee *et al.*, 2004). Nozzle entrainment has similarly been detected in precessing jet flows (Wong *et al.*, 2003). Visual evidence for the recirculation of particles occurring here is provided in Figure 4.10. Since the particles are only introduced through the annulus, they can only reach the centre of the nozzle exit plane by recirculation. These particles may be drawn into the OJ nozzle by the sub-atmospheric pressure within the chamber. This issue is believed to have some further consequences for nozzle performance and is discussed in more detail below. Figure 4.10 also shows the presence of large scale turbulent eddies and particle clustering found by Smith (2000) in a particle-laden PJ flow.
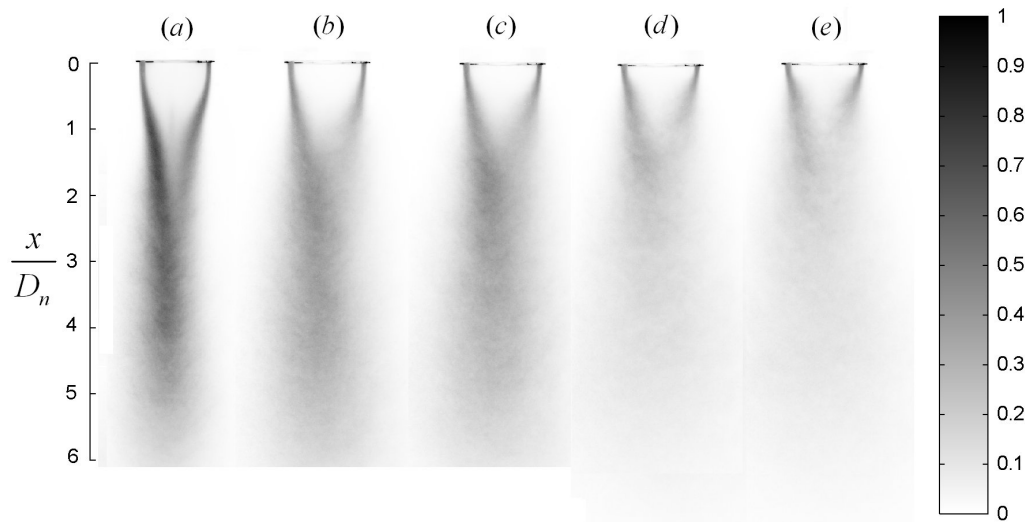
Figure 4.9: Mean images of particle distributions for (a) $G_1/G_2 = 0$, $\phi_o = 0.12$, (b) $G_1/G_2 = 0.3$, $\phi_o = 0.13$, (c) $G_1/G_2 = 0.9$, $\phi_o = 0.13$ (d) $G_1/G_2 = 3.7$, $\phi_o = 0.12$ and (e) $G_1/G_2 = 6.1$, $\phi_o = 0.09$.
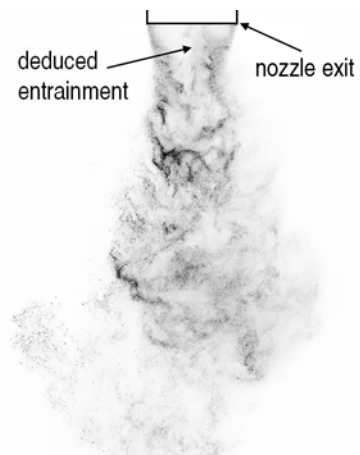

Figure 4.10: Single raw image, $G_1/G_2 = 6.1$, $\phi_o = 0.51$, showing the presence of particles on the nozzle axis immediately downstream from the exit plane. This is deduced to imply the entrainment of particles inside the nozzle chamber.
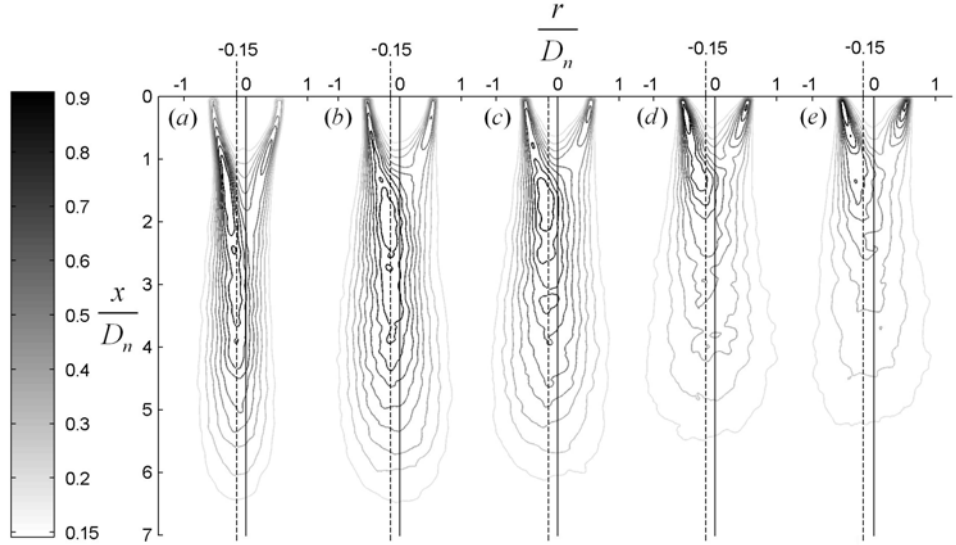
Figure 4.11: Contour plots of the mean images (Figure 4.9). Also shown is the apparent jet axis, at $r/D_n = $ -0.15 (dashed line).

The mean images of Figure 4.10 are re-presented as contour plots in Figure 4.11. A circular 10 point, two-dimensional, moving average, 'pillbox' filter is used firstly to reduce noise from the mean images. As discussed above for the case $G_1/G_2 = 0$, it can be seen that attenuation is most marked in the neck region ($x/D_n \approx 2$), i.e. at the narrowest part of the flow. Downstream, the flow converges to an axis left of the centreline as discussed above with reference to Figure 4.7, and indicated as $r/D_n = $ -0.15 in Figure 4.11. Judging by the symmetry of the contours about $r/D_n = $ -0.15, attenuation does not appear to be significant beyond $x/D_n \approx 3$ for all G_1/G_2. Once more, the effect of increasing the jet momentum on enhancing the spread of the solid phase is evident.

Exit profiles, S_o, normalised by the maximum signal S_{max}, for all momentum ratios are shown in Figure 4.12(a). As expected, strong peaks are found immediately downstream from the annular gap through which particles are conveyed. However, the peak on the weak side is some 10% greater than that on the strong side. To explain this finding, Figure 4.12(b) presents the locus of r_{max} over a much smaller axial range than was presented earlier in

Figure 4.7. It is clear that r_{max}/D_n undergoes a transition from the weak side to the to the strong side over the range $0.05 < x/D_n < 0.3$, consistent with the influence of nozzle misalignment (Figure 4.6). This is because, assuming an azimuthally uniform particle distribution, the number density is distributed over a smaller area. The profile in Figure 4.12(a) also shows that the concentration of particles in the central region is greatest for the bluff body recirculation case, $G_1/G_2 = 0$. The effect of G_1/G_2 on instantaneous recirculation is seen in Figure 4.12(c), where the scale of the ordinate of Figure 4.12(a), has been modified to highlight differences in the concentration in the central region. Figure 4.12(c) shows that S_o within the central region increases with G_1/G_2. Since particles only enter to this region by recirculation, the proportion of particles entrained into the nozzle must depend on G_1/G_2. This is further supported by manual inspection of individual images for the case $G_1/G_2 = 0.3$, relative to those for the case $G_1/G_2 = 6.1$. Whereas the entrainment of particles into the nozzle is rather obvious as highlighted in Figure 4.10, it is less for the case $G_1/G_2 = 0.3$.

Contour plots are presented in Figure 4.13 for the case $G_1/G_2 = 6.1$, each at a similar value of ϕ_o. Each exhibits a peculiar asymmetry in particle distributions as is highlighted by the straight lines of best fit through the loci of maximum signal, r_{max}/D_n. For example, the particles are preferably distributed to the left of the centreline for the case in Figure 4.13(a), to the right for the case displayed in Figure 4.13(c), while the case in Figure 4.13(b) is reasonably symmetric for $x/D_n > 3$. Although this inconsistent distribution of particles is evident for other G_1/G_2 (and for all ϕ_o), it is most readily observed for the case of maximum spread, $G_1/G_2 = 6.1$.

An insight into a possible explanation for the results of Figure 4.13 is obtained in Figure 4.14, which shows the exit profiles of the same cases as those displayed in Figure 4.13, for two levels of magnification. Although the exit profiles appear fairly similar, closer inspection reveals subtle differences. Firstly, the case $\phi_o = 0.09$ (Figure 4.13a) has a strong side peak with a magnitude that is slightly lower than for the case $\phi_o = 0.09$ (Figure 4.13b). Secondly, the signal within the recirculation region shown in more detail in
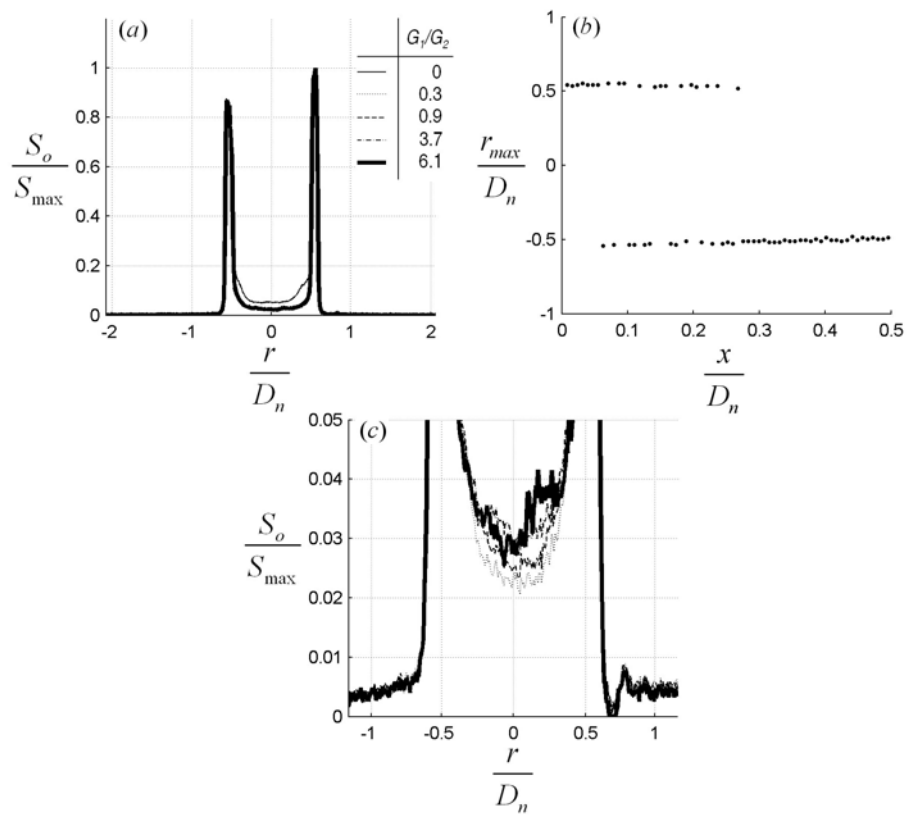
Figure 4.12: (a) Exit radial profiles ($x/D_n = 0$, $\phi_o = 0.12$), (b) loci of maximum signal (originally presented above in Figure 4.7a) for the range $0 < x/D_n < 0.5$ and (c) exit profiles with a different scale to highlight the central region.
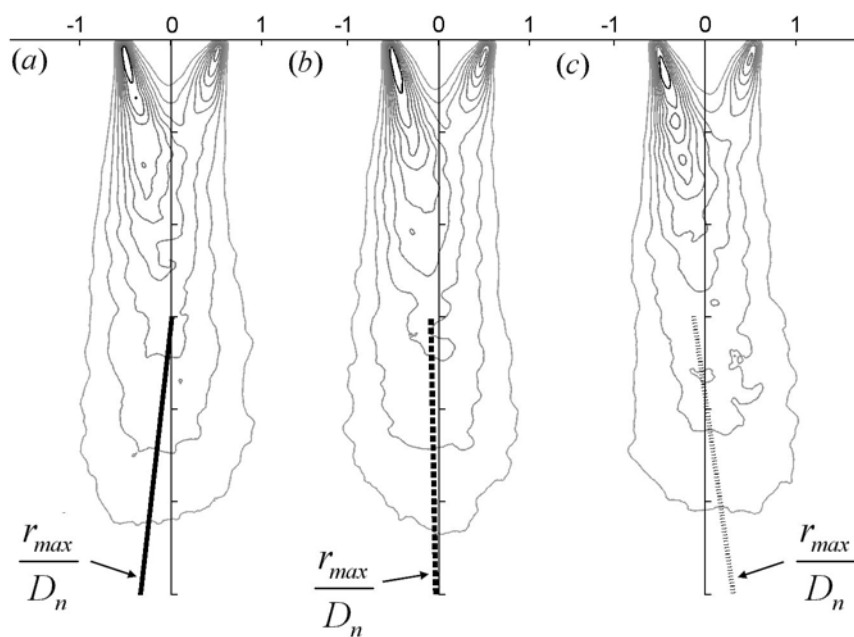
Figure 4.13: Contour plots for the case $G_1/G_2 = 6.1$ (a) $\phi_o = 0.09$, (b) $\phi_o = 0.09$, (c) $\phi_o = 0.07$ including best fitting lines of maximum signal, r'/D_n for the axial range $3 < x/D_n < 6$ (The contrast in this figure has been enhanced relative to that displayed in Figure 4.11(e) to assist visual inspection).
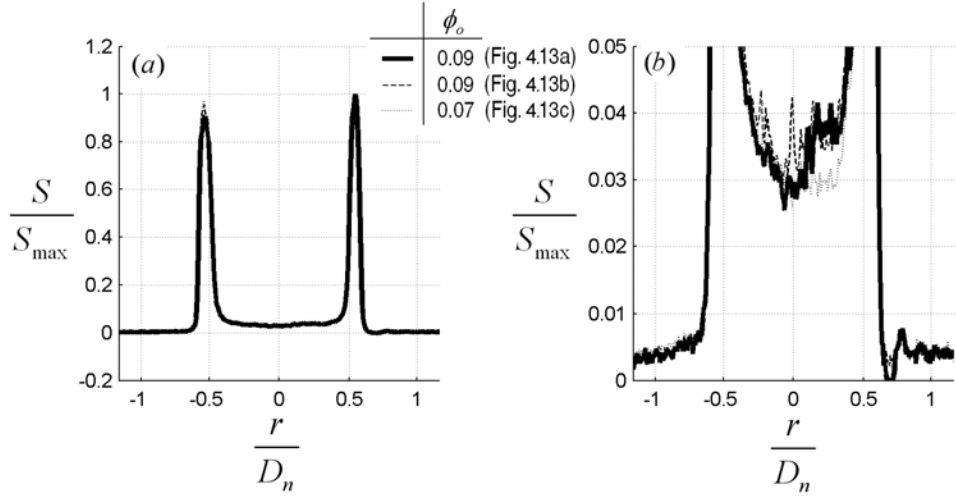
Figure 4.14: (a) Mean exit profiles for the case $G_1/G_2 = 6.1$ corresponding to the cases presented in Figure 4.13 and (b) magnified to show the difference in entrainment for each run.

Figure 4.14(b) differs between individual cases. Above (Figure 4.12a), the magnitude of S_o varied with G_1/G_2, whereas here, the shape mostly varies. For example, the case $\phi_o = 0.09$ (Figure 4.14a) has a greater concentration on the weak side within the entrainment region. Since entrainment will occur on the side opposite to that where the instantaneous jet emerges (Lee *et al.*, 2004), this implies that, on the mean, the jet favoured the strong side more often and can explain the orientation of r', and the shape of the contours, as displayed in Figure 4.13(a).

Although the cause for this variability is uncertain, two possible explanations have been identified. Firstly, it is possible that a random asymmetry is present in the initial particle distributions that are a result of the initial nozzle asymmetry (Figure 4.6). Secondly, a slight build-up of particles within the nozzle chamber, following their entrainment into the nozzle, may be affecting the oscillation. Whereas for a clean nozzle, the exit probability distribution is determined by the alignment of the triangle (Figure 4.1), any deposits of particles in the nozzle can be expected to bias the flow within the nozzle and, correspondingly, the emerging oscillating jet. For reference,

it is noted that the probability of this asymmetry being caused by aliasing with respect to the jet's frequency of oscillation is negligible. For 200 images per run (sampled at 10Hz) to be explained by aliasing, the jet oscillating frequency would have to be within 0.001% of the Nyquist frequency. Furthermore, the jet's frequency would have to occupy a narrow band, which it does not. Spectral measurements indicate the jet's frequency spectrum is broad (Lee *et al.*, 2003).

To compensate for the variable initial distribution of particles (Figure 4.14) and as a presumed result, the variable orientation of particle distributions downstream from the exit (Figure 4.13), half widths, $r'_{1/2}$, are calculated based on a line of best fit through the loci of maximum signal, r_{max}, i.e.

$$r'_{1/2} = r_{max}(S = S_{max}) - r(S = 1/2S_{max}) \qquad (4.4)$$

This differs from the half widths calculated in the usual way, i.e.

$$r_{1/2} = r(S = S_c) - r(S = 1/2S_c), \qquad (4.5)$$

where S_c are centreline values.

4.4 Centreline decay and spreading rates

The axial distribution of normalised signal on the jet centreline and half widths are presented in Figures 4.15(a) and (b), respectively. The inverse centreline signal is displayed in Figure 4.15(c). Centreline values, S_c, for all cases are obtained through the adjusted centreline, -0.15r/D_n, and are normalised by $S_{o,a}$, the signal obtained across the exit of the annulus alone. In contrast to the rapid, non-linear decay of 'apparent centreline concentration' as seen in Figure 4.15(c), half widths are found to be linear to within at least 90% in the range $3 < x/D < 6$ for all cases. From Figure 4.15(a), it can be seen that as G_1/G_2 is increased, the magnitude of the peak in

apparent centreline concentration is reduced and its axial location, denoted x_n, is translated closer to the origin. At the same time, half widths are increased by as much as a factor of two (Figure 4.15b) for this same increase in G_1/G_2. Also, the loci of maximum signal r_{max}/D_n is skewed slightly to the strong side for reasons already discussed. A comparison between x_n measured here and by Birzer *et al.* (2005) in a particle-laden PJ flow is displayed in Figure 4.15(d). Typically, it is desired in cement kilns to have the 'peak heat release' close to the burner since this improves overall efficiency as the kiln is a counter-flow heat exchanger (Manias & Nathan, 1994). Smith *et al.* (1998a,b) showed that, for the PJ nozzle, the increase in jet spread was associated with a four fold reduction in ignition distance and a shift in the hear release closer to the burner. This trend can be expected to follow for the OJ flow. A comparison between the two flows shows that x_n is consistently closer to the origin in the OJ compared with the PJ.

Since the extent to which these 'constants' may extend into the far field is yet to be assessed, they are termed near-field spreading coefficients, $K_{2,n}$. These are compared for the OJ and PJ over the range $3 < x/D_n < 6$. The PJ data are obtained from Birzer *et al.* (2005). The mass loading and the exit Stokes numbers are of the same order of magnitude for both flows. Because the OJ radial profiles are asymmetric (Figure 4.15b), $K_{2,n}$ is defined as the mean of the strong and weak side, i.e.

$$K_{2,n} = 1/2 \left(K_{2,s} + K_{2,w} \right) \tag{4.6}$$

where $K_{2,s}$ and $K_{2,w}$ are the strong and weak side near field spreading coefficients, respectively. As symmetry is assumed of the PJ flow, half widths for that case are defined as the distance between the centreline and a value half of that on the strong side only, i.e. $K_{2,n} = K_{2,s}$. The spreading rates of both flows are plotted in Figure 4.16(a) against the momentum ratio. It is found that $K_{2,n}$ depends approximately linearly on G_1/G_2 over the range $0 \lesssim G_1/G_2 \lesssim 6$ for both jets. Specifically, for the PJ,

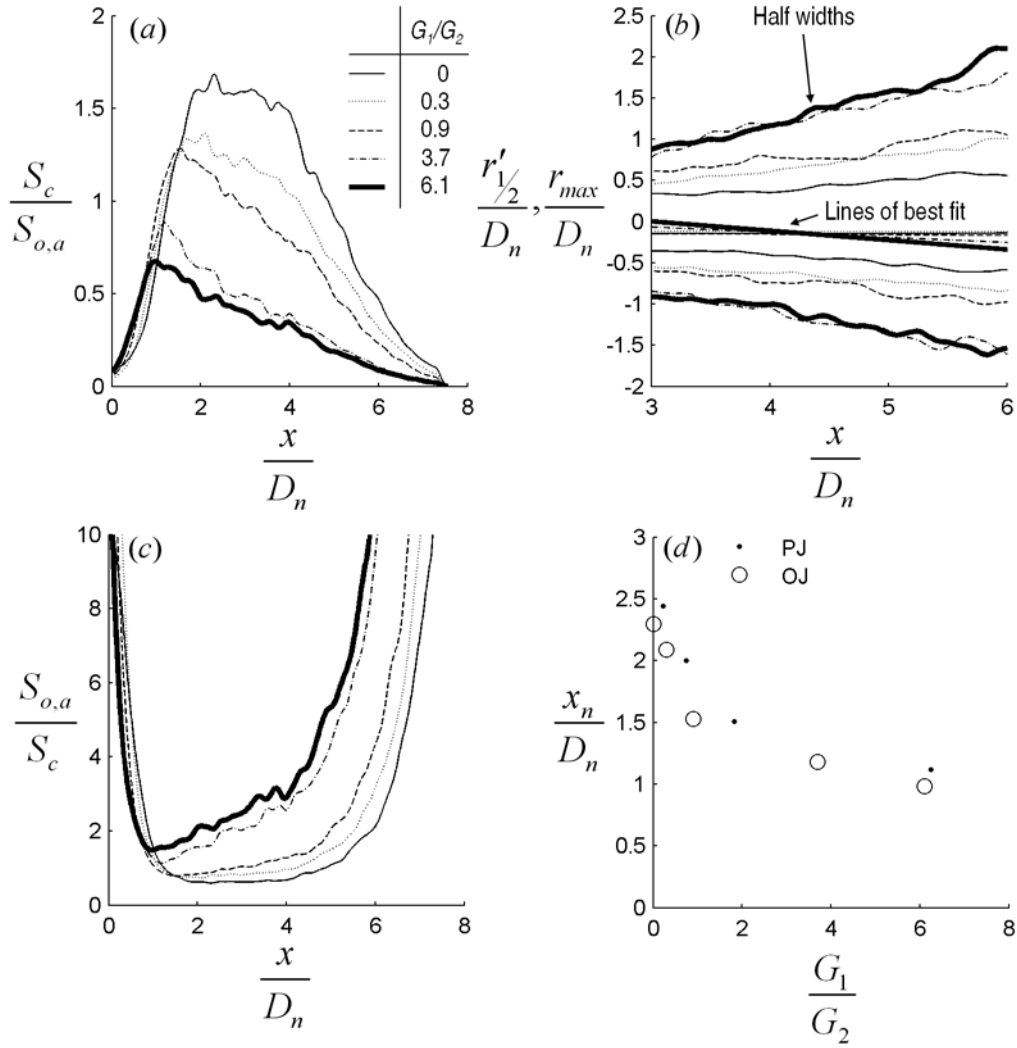$$K_{2,n} = 0.094 G_1/G_2 + 0.05 \tag{4.7}$$

Figure 4.15: (a) Centreline particle distributions normalised by the exit signal of the annular flow, (b) half widths relative to loci of maximum signal, r_{max}/D_n, (c) Inverse centreline particle distributions and (d) axial location of peak apparent centreline concentration, x_n.
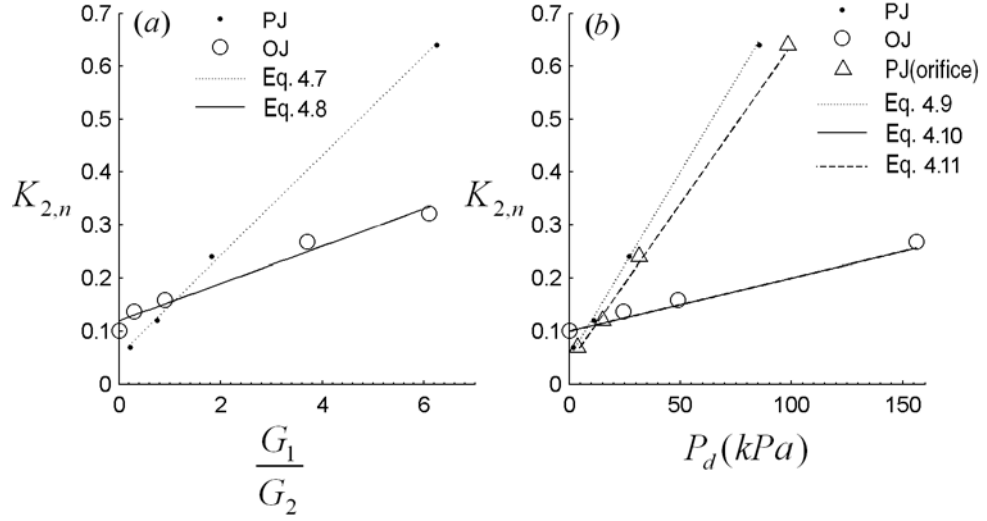
Figure 4.16: Comparison between PJ and OJ near field spreading coefficients, $K_{2,n}$ for a variation in (a) G_1/G_2 and (b) P_d. Linear trends are included according to equations 4.7-4.10.

and for the OJ,

$$K_{2,n} = 0.035G_1/G_2 + 0.12 \tag{4.8}$$

These equations are presented in Figure 4.16(a) with the data. The slope of these lines are almost a factor of three greater for the PJ than for the OJ. This is consistent with the finding of Lee *et al.* (2003) that the basic PJ nozzle produces a greater near field spreading rate than the OJ nozzle. However, for $G_1/G_2 \lesssim 1$, the spread of the OJ is greater than that of the PJ, consistent with the OJ having a lower momentum loss through the nozzle than the PJ.

Figure 4.16(b) presents the same data in terms of the driving pressure, P_d. Spreading coefficients for the PJ are described by

$$K_{2,n} = 0.007P_d + 0.05 \tag{4.9}$$

and the OJ,

$$K_{2,n} = 0.001P_d + 0.1 \tag{4.10}$$

Again, the OJ provides greater spread at pressures less than about 10kPa, while the PJ provides greater spread at higher pressures, which is also consistent with the lower loss coefficient of the OJ nozzle, compared with the PJ (Lee *et al.*, 2003). It is expected that the driving pressure of the OJ nozzle could be further reduced if a smooth contraction is used, although its shape may be complex, prior to the triangular orifice as has been done for the PJ nozzle for data reported by Birzer *et al.* (2005). The driving pressure P_d has also been measured for the case whereby the smooth contraction is replaced with an orifice plate in the PJ nozzle, with the assumption that jet spread will be equivalent to the smooth contraction case, which is approximately true (Wong, 2005). These results are also plotted in Figure 4.16(b), and described by

$$K_{2,n} = 0.006P_d + 0.04 \tag{4.11}$$

This shows that approximately 30% more supply pressure at the lower pressure range is required for the orifice case than the contraction case. A well designed smooth contraction prior to the triangular orifice would similarly improve performance relative to pressure drop.

In summary, these results identify that the OJ offers practical advantages for cases where the supply pressure is less than about 10kPa, a pressure which can be obtained with a fan. Importantly, previous trials with combustion using a PJ nozzle (Nathan & Hill, 2002, Smith *et al.*, 1998) showed that significant benefits can be achieved for $G_1/G_2 \approx 1$, which is the range where the OJ is more effective.

4.5   The effect of mass loading, ϕ_o

The influence of the exit mass loading, ϕ_o on distributions of particles is considered firstly for the case $G_1/G_2 = 0$ and then for the case $G_1/G_2 = 6.1$. Figure 4.17(a) presents the distribution of apparent centreline concentration for a range of values of ϕ_o, where it is found that the value of $S_c/S_{o,a}$ increases
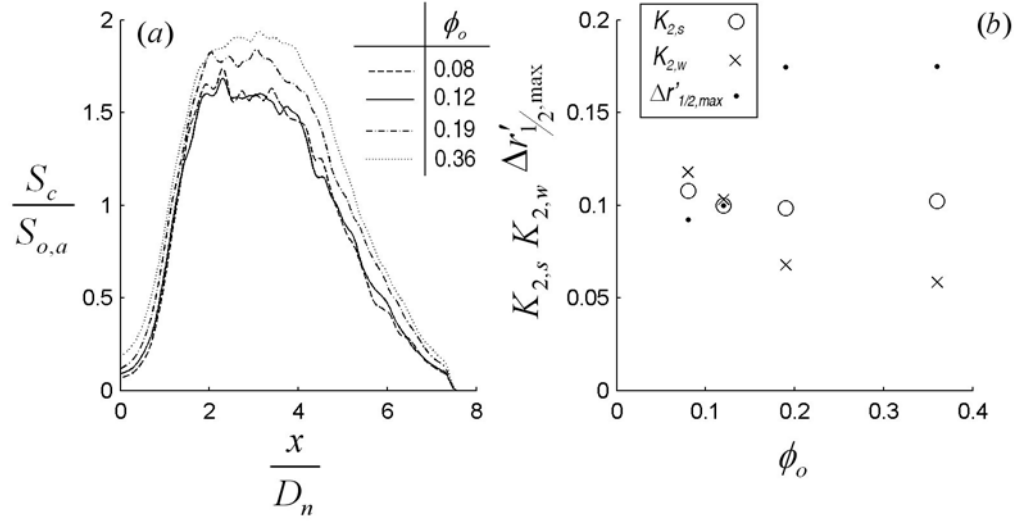
Figure 4.17: The influence of ϕ_o on (a) the centreline signal and (b) strong side, $K_{2,s}$, weak side, $K_{2,w}$ spreading rates and the maximum difference in half widths as calculated according to equation 4.3 for the case $G_1/G_2 = 0$.

with ϕ_o. Figure 4.17(b) presents the spreading constants on the strong $(K_{2,s})$ and weak $(K_{2,w})$ sides, as well as the maximum difference in half widths $(\Delta r_{1/2,max})$, where $r_{1/2}$ is calculated according to equation 4.3. For example, the maximum value of $\Delta r_{1/2}$ for the case $\phi_o = 0.12$, as originally displayed in Figure 4.8, is approximately 10%, which equates to a value of approximately 0.1 as shown in Figure 4.17(b). As expected, $\Delta r_{1/2,max}$, an indicator of the effects of attenuation, increases with ϕ_o. It is found therefore, that the weak side spreading rates, $K_{2,w}$, are reduced by an increase in ϕ_o. In contrast, $K_{2,s}$, which is less sensitive to light sheet attenuation, is approximately constant with variation in ϕ_o. The lack of influence of the solid phase on $K_{2,s}$ and hence, the characteristic flow length scale, is consistent with the mean exit Stokes number being in the regime where particles respond well to the large scale eddies in the flow. At this St_o, the effects of turbulence damping are expected to be small and so the characteristic length scale is largely unmodified by the addition of a solid phase.

The rise in the apparent centreline concentration with ϕ_o, also corre-

sponds to the rise in signal within the recirculation region as displayed in the exit profiles of Figure 4.18(a). It can be inferred from this figure that the proportion of particles within the recirculation zone increases with ϕ_o. Still more evidence for this is found in Figure 4.18(b). There, the centreline exit signal, $S_{o,c}$, normalised by the strong side peak, $S_{o,s}$, is plotted against ϕ_o, with $S_{o,c}$ being approximately proportional to ϕ_o. This can be explained by reference to the large eddy recirculation time scale for a bluff body flow which, after Borée *et al.* (2001), is defined as

$$\tau_{rec} = \frac{2D_n}{U_{2,max}}. \tag{4.12}$$

It can be seen that in this definition of the flow timescale, the velocity is the *maximum* velocity at the exit, $U_{2,max}$, as opposed to the bulk mean velocity, U_2 used in the definition of equation 4.2. It is a well known phenomena in particle-laden turbulent axisymmetric jets that as ϕ_o increases, gas phase velocity profiles are 'flattened' (Hardalupas *et al.*, 1989). Hardalupas *et al.* (1989) have reported a reduction in centreline velocity at their jet exit by some 20% for $\phi_o = 0.86$ ($\tau_p = 11.9$ms), relative to the single phase case. Although data is presented here in the absence of velocity measurements, a flattening of the exit velocity profile is expected here within the annular channel. As a consequence, the entrainment of particles into the recirculation region may be increased, since $St_{o,rec}(= \tau_p/\tau_{rec})$ is reduced for an increase in ϕ_o. This may explain, at least partly, the results in Figure 4.17(a) and 4.18. Although the linear increase in $S_{o,c}/S_{o,s}$ in Figure 4.18(b) is reported for that range of ϕ_o, it would be expected to asymptote with further increases in ϕ_o as the gas phase exit velocity approaches a top-hat profile.

Centreline values for the case $G_1/G_2 = 6.1$ are shown in Figure 4.19(a) for a range of ϕ_o. The effects of attenuation appear to be significant in the range $x/D_n < 2$ because the centreline values of the case $\phi_o = 0.51$ correspond closely with the case $\phi_o = 0.41$ in that region. Further downstream, it follows a trend that is consistent with the other cases. This also suggests that the effects of attenuation are not very significant in the region $x/D_n > 3$,
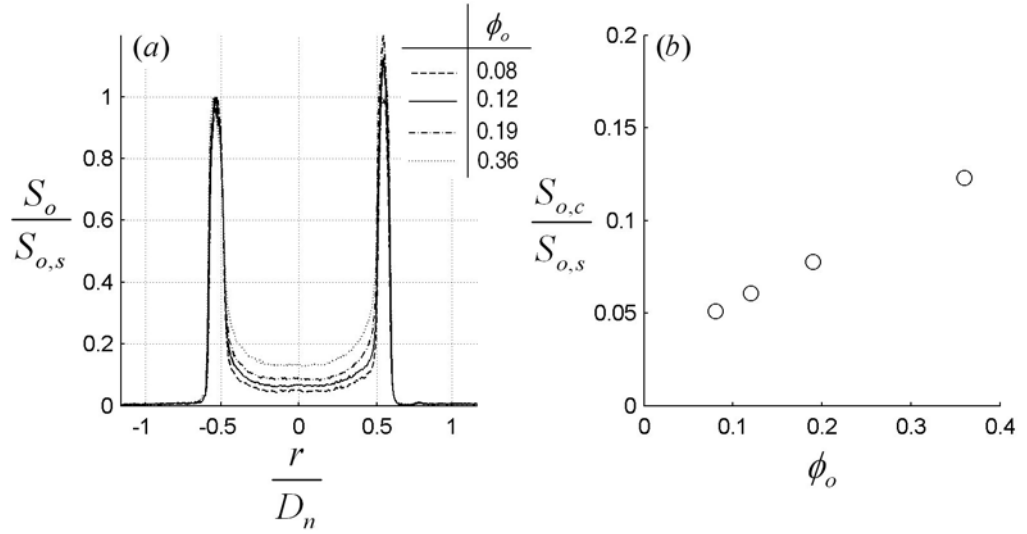
Figure 4.18: (a) Exit profiles and (b) centreline exit values, $S_{o,c}$, for a variation in exit mass loading, ϕ_o for the case $G_1/G_2 = 0$.

where mean near field spreading constants are assessed below for a variation in ϕ_o. As was found for the case $G_1/G_2 = 0$, an increase in the apparent centreline concentration with ϕ_o is detected. Its cause may also be attributed to the increase in particle recirculation with ϕ_o, as evidenced by the rise in magnitude of the exit signal with ϕ_o within the recirculation region in Figure 4.19(b). As in Figure 4.18(b), the increase in $S_{o,c}/S_{o,s}$ is approximately proportional to ϕ_o (Figure 4.19c). As discussed above however, the entrainment mechanism here is different from that of the bluff body flow.

Half widths for the case $G_1/G_2 = 6.1$ are shown in Figure 4.20(a) for a range of ϕ_o. Also presented is r'_{max}, following Figure 4.13(b). It can be seen that r'_{max} for these cases are distributed on both sides of the pipe centreline. The mean spreading constants are plotted in Figure 4.20(b) against ϕ_o. In contrast to the case $G_1/G_2 = 0$ above, there is an almost linear dependence of K_2 on ϕ_o, with spread decreasing for an increase in ϕ_o. Two possible explanations for this effect are identified. Firstly, an increase in ϕ_o corresponds to a reduction in G_1/G_2. Borée *et al.* (2001) showed in their bluff body study, that the addition of particles to the jet stream gives a 'global'

momentum ratio equal to $G_1(1 + \phi_o)/G_2$. As a result, their central jet was able to penetrate through the recirculation region by virtue of its additional momentum. Since particles are conveyed by the annular channel here, the 'global' momentum ratio is equal to $G_1/G_2(1 + \phi_o)$ and so the influence of the OJ is correspondingly weakened with respect to the annular flow, for an increase in ϕ_o.

Secondly, the reduction in spread with increased ϕ_o could also be a function of particle-fluid interaction within the nozzle. To better explain this result, we refer to the measurements of England *et al.* (2005). They showed that the near-field spreading angle of a single phase jet from the same OJ nozzle, decreases with an increase in the density of the jet fluid. That particle entrainment into the nozzle detected here will effect the spread is therefore consistent with the optimal nozzle geometry being altered as found by England *et al.* (2005). In contrast to England *et al.* (2005) however, the two phase interaction between particles and the flow in the nozzle will include turbulence damping and other momentum exchange effects and even particle agglomeration within the nozzle as discussed above. However, as deduced from Figure 4.12(c), the relative particle entrainment into the nozzle is reduced by a reduction in G_1/G_2. This suggests that these influences will become less important as G_1/G_2 is reduced.

It is unlikely that turbulence modulation is a significant cause of the reduced spread in Figure 4.20. This is because St_o is even lower for the OJ flow than for the basic annular jet due to the lower values of τ_f in a precessing jet flow (Nathan *et al.*, 1998). Hence, the particles should follow the flow even better for $G_1/G_2 = 6.1$, than for the case $G_1/G_2 = 0$. Furthermore, from equation 4.1, ϕ_o was calculated on the basis of the fluid mass flow through the annulus alone. If the mass of the fluid through the OJ nozzle were included, i.e. the 'global' mass loading, then this would further reduce the magnitude of ϕ_o, thus reducing any effects of turbulence modulation further. For example, the global mass loading for the case $\phi_o = 0.51$, $G_1/G_2 = 6.1$, is 0.19.
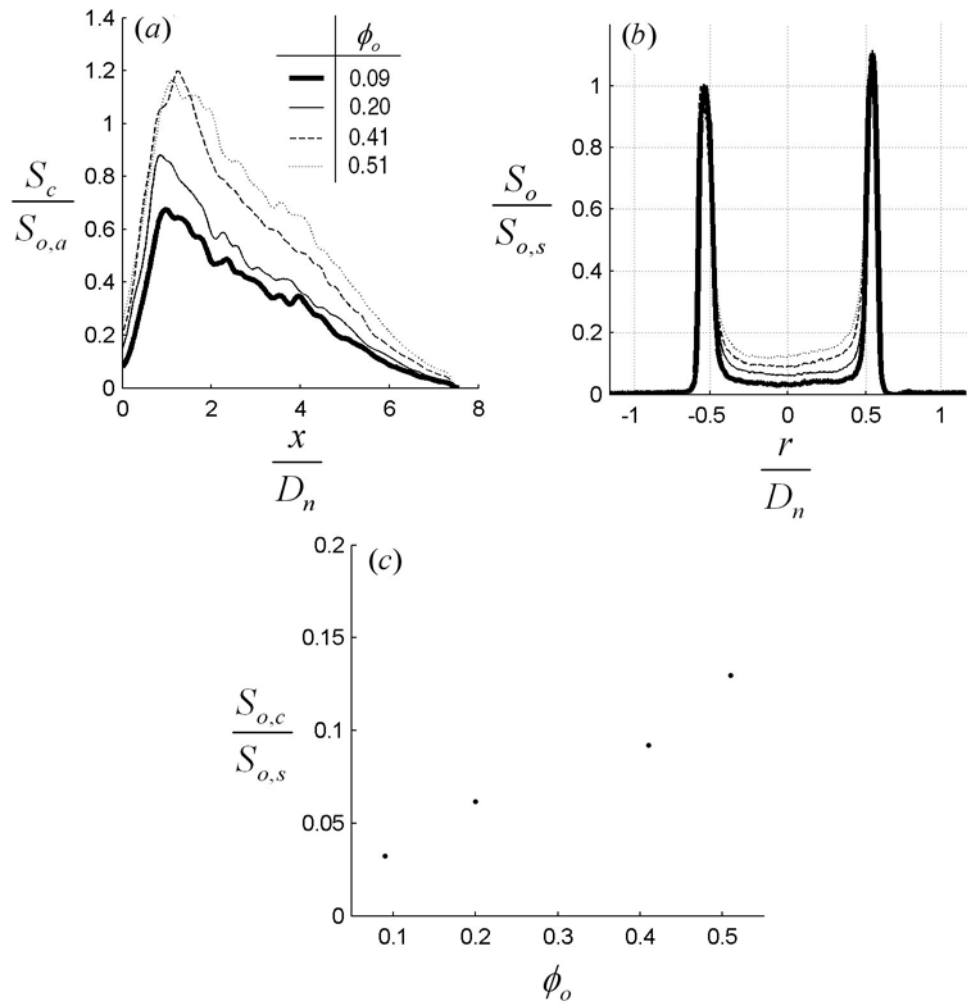
Figure 4.19: (a) Centreline values, (b) exit profiles and (c) centreline exit values for the case $G_1/G_2 = 6.1$ as a function of ϕ_o.
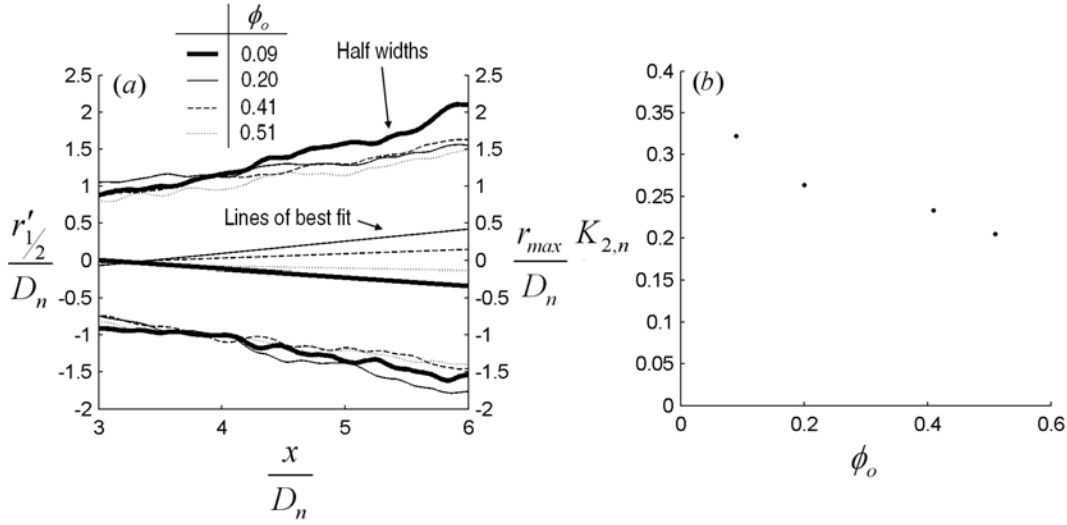
Figure 4.20: (a) Half widths based on loci of maximum signal, r_{max}/D_n for the case $G_1/G_2 = 6.1$ and (b) the mean spreading constant plotted against ϕ_o.

4.6 Conclusions

Measurements of the distribution of particles, introduced via an annular channel, in a particle-laden triangular oscillating jet flow were performed. The momentum ratio (G_1/G_2) of the oscillating jet to that of the annular channel was varied, as was the exit mass loading ϕ_o, the ratio of the mass flow of particles through the channel to that of the air. The near field spreading coefficient $K_{2,n}$ of particle distributions in an OJ flow was found, similarly to that found in a comparative PJ flow, to be linear with axial distance, x/D_n. The rate of increase in $K_{2,n}$ with G_1/G_2 is greater for the PJ compared with the OJ, consistent with the greater absolute spread of the PJ flow, without the presence of an annular stream. However, for $G_1/G_2 \lesssim 1$, the $K_{2,n}$ of the OJ exceeds that of the PJ. This equates to a greater OJ spread for driving pressures P_d less than approximately 10kPA, which can be obtained by fans at industrial scale.

For constant $G_1/G_2 = 0$, an increase in ϕ_o leads to increased recirculation.

This is because the velocity profiles within the annular channel approach a top-hat shape (i.e. they are 'flattened') for an increase in ϕ_o. Consequently, the time-scale for recirculation, defined as the ratio of twice the nozzle diameter to that of the maximum exit velocity $(2D_n/U_{2,max})$, is reduced, and particles are more ably entrained into the recirculation region by virtue of their reduced Stokes number. For constant $G_1/G_2 = 0$, $K_{2,n}$ is independent of ϕ_o, consistent with negligible turbulence damping.

For constant $G_1/G_2 = 6.1$, the recirculation is similarly increased with ϕ_o. However, the entrainment mechanism in this case is a consequence of the sub-atmospheric pressure within the nozzle. For constant $G_1/G_2 = 6.1$, $K_{2,n}$ is approximately linearly dependent on ϕ_o. The large-eddy length scale is known to increase in oscillating flows, which correspondingly reduces the Stokes number. For that reason, turbulence damping is even less likely to be significant for $G_1/G_2 = 6.1$ compared with the case $G_1/G_2 = 0$. The reduction in $K_{2,n}$ with ϕ_o is therefore a likely consequence of the reduction in the global momentum ratio as well as the entrainment of particles within the nozzle. Measurements by previous authors suggests that the optimum nozzle geometry and hence jet spread, are affected for flows with different density.

Chapter 5

Conclusions

A survey of measurements reported in the literature, as well as independent measurements conducted in this thesis, have further highlighted the importance of Stokes number and mass loading effects on the behaviour of particle-laden steady and unsteady jets. Both the Stokes number and the mass loading determine the relative importance of turbulence modulation and interphase momentum exchange in these flows. For example, for very high Stokes numbers $St_o \gtrsim 200$, it was found in Chapter 2 that gas phase centreline velocity measurements in particle-laden axisymmetric jets reported by previous authors, scale with $x/D(1 + \phi_o)^{-1/2}$, while half widths were found to be approximately independent of ϕ_o. Momentum exchange effects are important for high Stokes numbers, since particles with a high inertia act as a source of momentum for the gas phase. As the Stokes number is reduced, particles are more able to respond to turbulent fluctuations which results in a damping action of the gas phase turbulence. For intermediate Stokes numbers, $20 \lesssim St_o \lesssim 200$, centreline velocities collapse if scaled with $x/D(1 + \phi_o)^{-1}$, while half widths collapse when scaled with $x/D(1 + \phi_o)^{-1/2}$. In this regime, particles are partially responsive to turbulent fluctuations, yet a mean slip velocity still exists. Hence, both interphase momentum exchange and turbulence damping are considered important in this regime. As the Stokes number is further reduced, the effects of mean interphase momen-

129

tum transfer become negligible as particles are more able to follow the flow. This subsequently increases the effects of turbulence damping as particles are able to extract a greater portion of kinetic energy from the gas phase. For low Stokes numbers, $St_o \lesssim 20$, centreline velocities and half widths collapse if scaled by $x/D(1 + \phi_o)^{-1}$.

In addition to the scaling of gas phase, previously reported solid phase mass flux and concentration measurements were found to scale similarly to the gas phase. Measurements of half widths obtained from particle distributions using a planar imaging technique were found to collapse, although somewhat ambiguously, when scaled with $x/D(1 + \phi_o)^{-1/2}$ in Chapter 3. The ambiguity was concluded to partly result from the polydisperse particle size distribution. The cause for the independence of centreline distributions from mass loading was also attributed to particle polydispersity, since a large number of particles in the flow are unresponsive to the gas phase for a large part of the measurement region. For very low Stokes numbers, the effects of turbulence damping become less significant since small particles are easily accelerated by the gas phase and the turbulence transfers minimal kinetic energy to the particles.

A similar planar imaging technique to that performed in Chapter 3 was used to measure the distribution of particles delivered via an annular channel, in an unsteady flow - the triangular oscillating jet. As the Stokes number in this study was sufficiently low, this led to the conclusion that turbulence damping was negligible. However, a reduction in the spread of particles with mass loading was nevertheless detected. This was attributed to the extra momentum through the annular channel for increasing ϕ_o, which resulted in a reduction to the 'global' momentum ratio. At constant ϕ_o, the spread of particles in the OJ flow was compared with the spread of particles in an analogous flow, the precessing jet. While the spread of particles in a PJ flow increases at a greater rate with momentum ratio, for $G_1/G_2 \lesssim 1$ and driving pressures less than approximately 10kPA, the spread of particles in an OJ flow is superior. It is at these conditions that the OJ is thought to be superior to the PJ.